



Nutrient transport and dynamics in the South China Sea: A modeling study

Zhongming Lu^a, Jianping Gan^{a,b,*}, Minhan Dai^c, Xiaozheng Zhao^a, Chiwing Rex Hui^b

^a Division of Environment and Sustainability, Hong Kong University of Science and Technology, Hong Kong

^b Department of Ocean Science and Department of Mathematics, Hong Kong University of Science and Technology, Hong Kong

^c State Key Laboratory of Marine Environmental Science, Xiamen University, Xiamen, China

ARTICLE INFO

Keywords:

South China Sea
Transport and dynamics
Model
Nutrient

ABSTRACT

The South China Sea (SCS) is one of the largest marginal seas in the world, yet the processes that drive its nutrient distribution are not well understood. Using the three-dimensional China Sea Multiscale Ocean Modeling System (CMOMS) embedded with a nitrogen-phosphorus-phytoplankton-zooplankton-detritus ecosystem model, we investigated nutrient transport and dynamics in the SCS. The model was well validated with field and remotely sensed observations. We found that the unique layered distribution of nutrients that increases from north to south in the upper layer and increases in the opposite direction in the middle and deep layers. We found that the lateral and vertical fluxes associated with three-dimensional ocean circulation and biogeochemical processes shape the distribution. The lateral fluxes are provided extrinsically by the sandwich-like transport through Luzon Strait (LS) and the exchanges through other straits, and intrinsically by the interior vertical motion due to flow-slope topography interaction. The nutrient deficiency in the upper layer due to dilution by inflow from the Western Pacific Ocean is mainly compensated by the upward nutrient-rich deep water. The nutrient transport is jointly regulated by volume transport and the uneven spatiotemporal distribution of nutrients. We demonstrated that labile organic matter plays an important role in total nutrient budgets. In euphotic layer, biological production is the major sink, but remineralization contributions to PO_4 are more important than to NO_3 due to the higher recycling rate of PO_4 . In the shelf water, coastal upwelling serves as major source for both NO_3 and PO_4 , vertical diffusion is another important source of PO_4 due to the strong downward increasing gradient.

1. Introduction

The South China Sea (SCS) is located within the tropical-subtropical rim of the western North Pacific Ocean and is among one of the largest marginal seas in the world with an area that measures approximately $3.5 \times 10^6 \text{ km}^2$ (Fig. 1). There is a wide shallow continental shelf (isobaths $< 200 \text{ m}$) sits in the northern and southwestern parts of the sea while the central region has a deep basin (Chai et al., 2009; Chen et al., 2001; Shaw and Chao, 1994).

The circulation in the SCS is complex and largely governed by the East Asian monsoon and the lateral transport through channels that connect the SCS to adjacent seas (Qu, 2000). The SCS exchanges water with the East China Sea (ECS) through Taiwan Strait (TS), with the Western Pacific Ocean (WPO) through Luzon Strait (LS), with the Sulu Sea through Mindoro and Balabac Strait (MS), and with the Java Sea through Karimata Strait (KS).

The basin-scale surface circulation responds to the northeasterly winter monsoon and the southwesterly summer monsoon with cyclonically and anti-cyclonically along-slope flow, respectively. In addition,

there is the surface Kuroshio intrusion through LS (Gan et al., 2006; Gan et al., 2016a; Qu, 2000). A unique three-layer cyclonic-anticyclonic-cyclonic (CAC) circulation operates vertically in the upper ($< 750 \text{ m}$), middle (750 to 1500 m), and deep ($> 1500 \text{ m}$) layers and is induced by the inflow-outflow-inflow structure in LS and the consequent vortex stretching in the SCS basin (Gan et al., 2016b).

Nutrient transport and dynamics in the SCS are complex because they are strongly influenced by circulation and associated spatial variability. Biological activities complicate the processes further in the upper layer. The exchange flow between the SCS and the WPO through LS provides the dominant nutrient flux for the SCS (Gan et al., 2016a; Wong et al., 2007b).

In the WPO, there is a nutrient maximum at a depth of $\sim 1000 \text{ m}$. However, the vertical distribution of nutrients in the SCS is much more uniform than in the WPO, and the concentration is considerably higher than in the WPO in the subsurface layer (100 to 600 m). The opposite is true in the intermediate layer (600 to 1500 m) of the SCS where there is stronger vertical mixing and upward advection (Gong et al., 1992).

Nutrient transport into and out of the SCS has been studied by many

* Corresponding author at: Department of Ocean Science and Department of Mathematics, Hong Kong University of Science and Technology, Hong Kong.
E-mail address: magan@ust.hk (J. Gan).

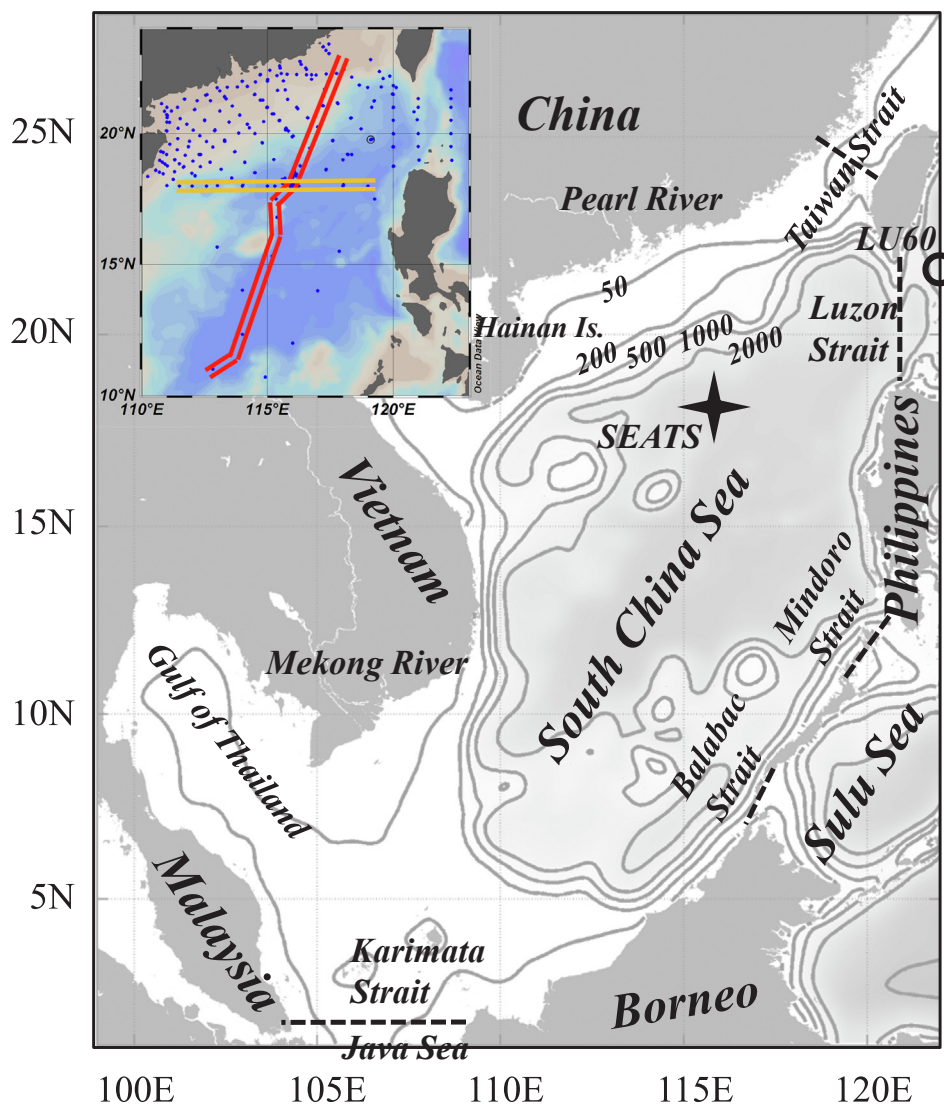


Fig. 1. Map of the South China Sea (SCS) with isobaths (m). The black star and the open circle indicate the locations of SEATS and the LU60 station respectively. The straits are indicated by black dashed lines. The blue dots on the small map at the top left corner indicates the stations from various cruises. The red and orange double lines represent the meridional and zonal sections for the observation - model comparison. (For interpretation of the references to color in this figure legend, the reader is referred to the web version of this article.)

researchers. For transport through LS, [Chen et al. \(2001\)](#) used a mass balance box model to estimate the nitrogen (N) and phosphorus (P) inputs through LS in the middle and deep layers. However, they could not separate the transport in upper layer from those contributed by other straits (such as TS and KS). Using an isopycnal mixing model, [Du et al. \(2013\)](#) found that the nutrient inventory in the upper 100 m of the SCS is negatively correlated with the extent of the Kuroshio intrusion. However, they warned that their method might not be valid when the timescale exceeds the water residence time and diapycnal mixing becomes significant. Using the same mass balance method as [Chen et al. \(2001\)](#) used, previous studies estimated the nutrient transport from the SCS to the ECS through TS to range from 22×10^9 to 203×10^9 mol yr⁻¹ for N and from 2.2×10^9 to 13×10^9 mol yr⁻¹ for P ([Liu et al., 2010a](#); [Zhang et al., 2007](#)). However, other studies suggested that the nutrient transport from the ECS to the SCS occurs due to a massive winter nutrient flux via the China Coastal Current (CCC) in winter ([Chen, 2008](#); [Han et al., 2013](#)). Nutrient transport through MS and KS has rarely been investigated, with one exception is a study by [Chen et al. \(2001\)](#) who reported a larger influx through MS (39×10^9 mol yr⁻¹ for N and 3.9×10^9 mol yr⁻¹ for P) and a smaller influx through KS (12×10^9 mol yr⁻¹ for N and 0 mol yr⁻¹ for P).

In the SCS basin, nutrients in the euphotic layer are supplied by vertical mixing and upward motion induced by the East Asian monsoon and various oceanic physical processes such as mesoscale eddies ([Zhou et al., 2013](#)). In the mixed layer of the SCS basin, unlike other low-latitude waters, the nutrient concentration varies significantly from season to season ([Wong et al., 2007a](#)). The highest nutrient levels and the strongest biological production in the mixed layer occur in winter when the strongest northeasterly monsoon prevails ([Chen, 2005](#)). Over the continental shelf, nutrient concentration is much higher and generally peaks during summer due to river runoff and coastal upwelling ([Chou et al., 2007](#); [Gan et al., 2006](#)). The nutrient input from the Mekong River and the Pearl River (world's 10th and 13th largest rivers in terms of discharge ([Dai and Trenberth, 2002](#); [Zhai et al., 2005](#))) is as high as 97×10^9 mol yr⁻¹ for N and 1.2×10^9 mol yr⁻¹ for P and exhibits significant seasonality. However, the contribution of nutrients by upward flux is still not completely determined ([Chen et al., 2001](#)). Over the northern shelf of the SCS, [Wong et al. \(2015\)](#) suggested that vertical mixing brings nutrients from the deep layer to the mixed layer in summer and winter. In winter, the offshore nutrient transport can be enhanced by the presence of a thermohaline front ([Liu et al., 2010b](#)). Unlike in the bioactive upper layer, nutrient concentration in the deep

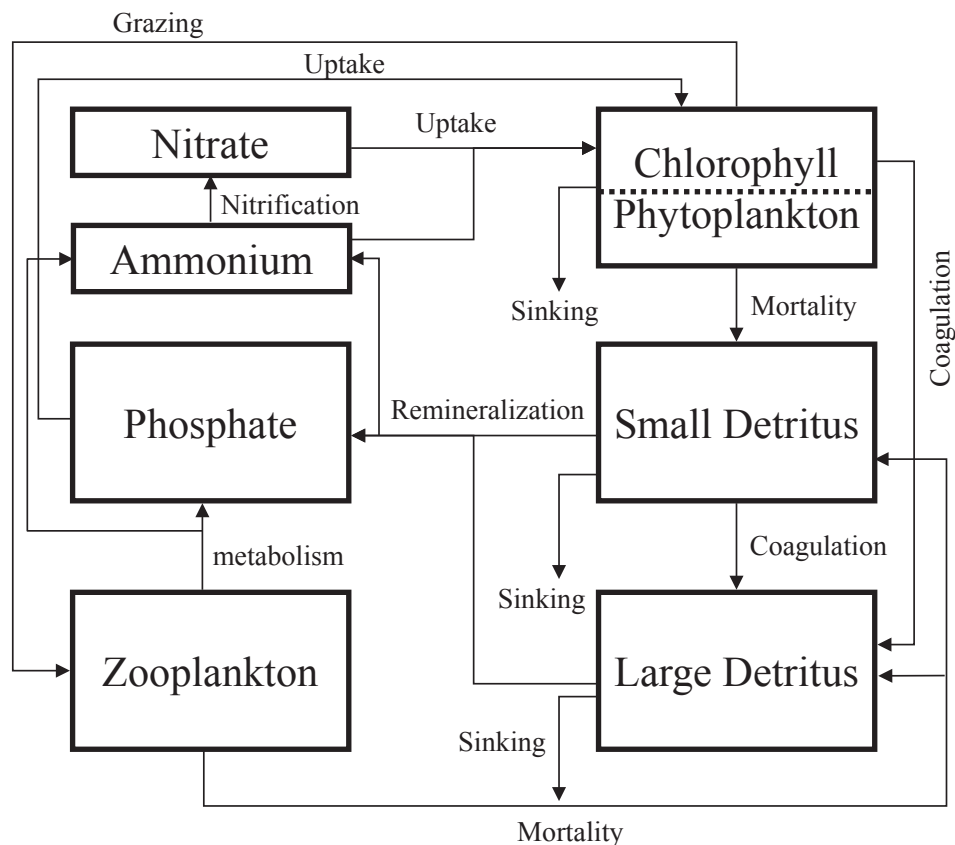


Fig. 2. Schematic diagram of the biological module of the model. Boxes represent different biological variables. Arrows indicate the biogeochemical processes [adopted from Gan et al., 2014].

layer of the SCS basin stays relatively constant over time (Wong et al., 2007a).

An understanding of the nutrient transport and dynamics is essential for quantifying the nutrient budget and revealing the biogeochemical processes of the SCS. However, the mechanisms and processes regulating the evolution of the SCS water are still poorly understood, which is mainly because we are lack of understanding about the three-dimensional circulation and transport besides the associated biogeochemical process in the SCS. Lacking comprehensive understanding of the time-dependent three-dimensional circulation in the SCS and the water exchange with adjacent seas often leads to misinterpretation and irrational speculation of the nutrient transport and dynamics. By focusing mainly on local phenomena in different parts of the SCS, as in most of the previous studies, we have overlooked the holistic interactions between physical and biogeochemical processes and between processes within and outside the SCS.

In this study, by combining observed data and a coupled physical-biogeochemical model, we explain the three-dimensional, time-dependent nutrient response to the physical circulation and biogeochemical processes in the SCS. This model-based study of the nutrient budget in the SCS, based on our recent finding of novel layered circulation in the SCS (Gan et al., 2016a, b; Liu and Gan, 2017), paints a complete picture of the nutrient distribution, transport, and dynamics in the SCS, thus paving the way for future studies.

2. Materials and methods

2.1. Ocean model and implementation

We used a coupled physical-biological model that is based on the China Sea Multiscale Modeling System [CMOMS, <https://odmp.ust.hk/cmoms/>, Gan et al., 2016a,b). CMOMS adopts the Regional Ocean

Modelling System (ROMS) (Shchepetkin and McWilliams, 2005) that describes three-dimensional, time-dependent circulation using the hydrostatic primitive equations. The biological part of the modeling system is a N-P based ecosystem model developed by Gan et al., 2014 that used the framework of the Fasham-type N-based ecosystem (Fasham et al., 1990; Fennel et al., 2006).

CMOMS integrates circulation in the estuaries, shelves, basins, and open oceans at different subscales. Our model domain extended from $\sim 0.95^{\circ}\text{N}$, 99°E in the southwest corner to $\sim 50^{\circ}\text{N}$, 147°E in the northeast corner. The model's horizontal coordinate system adopts a curvilinear grid. The horizontal resolution of our domain ranged from ~ 7 km in the north to ~ 10 km in the south with respect to a cylindrical map projection. Vertically, we adopted a 30-level stretched generalized terrain-following coordinate system with higher resolution in the surface and bottom layers than in the middle layer.

The model was initialized by climatological winter salinity and temperature from the World Ocean Atlas 2013 (WOA13). We forced the model with wind stress derived from the climatological monthly reanalysis of 10 m blended sea winds (averaged over 1981–2010) released by NOAA (<https://www.ncdc.noaa.gov/oa/rsad/air-sea/seawinds.html>), the data set has $0.25^{\circ} \times 0.25^{\circ}$ resolution. We used the atmospheric heat and salt fluxes from the climatological monthly NCEP (National Centers for Environmental Prediction) reanalysis 1 meteorological variables, the data set has $1.875^{\circ} \times 1.875^{\circ}$ resolution.

At the open boundaries, we applied a set of newly developed active open boundary conditions (OBCs) (Liu and Gan, 2016) to accommodate tidal forcing, subtidal forcing and climatological monthly discharges from the rivers surrounding the SCS (e.g., the Pearl River, the Mekong River, and the Red River).

The CMOMS successfully simulated the extrinsic forcing of coherent transports through the straits surrounding the China Seas. In addition, the model simulated the intrinsic circulation response of, for example,

Table 1
Biogeochemical model parameters.

| Description | Symbol | Value | Units |
|---|-------------|--------|---|
| Phytoplankton growth rate at 0°C | μ_0 | 3 | d ⁻¹ |
| Light attenuation due to seawater | k_{water} | 0.04 | m ⁻¹ |
| Light attenuation by chlorophyll | k_{Chla} | 0.025 | (m ² mg Chla) ⁻¹ |
| Initial slope of the P-I curve | α | 0.06 | mg C (mg Chla Wm ⁻² d) ⁻¹ |
| Maximum cellular chlorophyll : C Ratio | θ_m | 0.054 | mg Chla (mg C) ⁻¹ |
| Cellular P:N ratio | r_{PN} | 0.0625 | – |
| Half-saturation for phytoplankton NO ₃ uptake | k_N | 0.96 | mmol m ⁻³ |
| Half-saturation for phytoplankton. NH ₄ uptake | k_A | 0.96 | mmol m ⁻³ |
| Half-saturation for phytoplankton. PO ₄ uptake | k_P | 0.06 | mmol m ⁻³ |
| Phytoplankton mortality rate | m_{phyto} | 0.15 | d ⁻¹ |
| Zooplankton maximum grazing rate | g_{max} | 0.5 | d ⁻¹ |
| Zooplankton assimilation efficiency for Nitrogen | β | 0.75 | – |
| Zooplankton half-saturation constant for ingestion | k_{phyto} | 3.5 | mmol N m ⁻³ |
| Zooplankton basal metabolism | l_{BM} | 0.1 | d ⁻¹ |
| Zooplankton specific excretion rate | l_E | 0.1 | d ⁻¹ |
| Zooplankton mortality rate | m_{Zoo} | 0.025 | d ⁻¹ (mmol N m ⁻³) ⁻¹ |
| Small detritus remineralization rate for nitrogen | r_{SDN} | 0.03 | d ⁻¹ |
| Large detritus remineralization rate for nitrogen | r_{LDN} | 0.01 | d ⁻¹ |
| Small detritus remineralization rate for phosphorus | r_{SDP} | 0.075 | d ⁻¹ |
| Large detritus remineralization rate for phosphorus | r_{LDP} | 0.025 | d ⁻¹ |
| Coagulation rate | τ | 0.05 | d ⁻¹ |
| Sinking velocity for small detritus | w_{SD} | 0.1 | m d ⁻¹ |
| Sinking velocity for large detritus | w_{LD} | 1 | m d ⁻¹ |
| Sinking velocity for Phytoplankton | w_{phyto} | 0.1 | m d ⁻¹ |
| Maximum nitrification rate | n_{max} | 0.05 | d ⁻¹ |
| Threshold PAR for nitrification inhibition | I_0 | 0.0095 | W m ⁻² |
| Half-saturation PAR for nitrification inhibition | k_I | 0.036 | W m ⁻² |

alternating spinning layered circulation in the SCS. The extrinsically forced transports and intrinsic response are critical to the biogeochemical responses in the basin of the SCS. More details about the physical model are in Gan et al. (2016a,b).

The biological component of our coupled model is a NPPZD (nitrogen, phosphorus, phytoplankton, zooplankton, and detritus) model (Fig. 2). The NPPZD model reasonably reflects the P limitation resulting from the river plumes in the SCS. A detailed description of the biological model and the equations that govern the biological processes are in Gan et al., 2014. The parameters used in the NPPZD model are shown in Table 1. These parameters were derived from previous studies in the SCS (e.g. Gan et al., 2014) and in other oceans around the world (Fennel et al., 2006; Spitz et al., 2005). We set the NO₃ and PO₄ concentrations in river discharge to 90 mmol m⁻³ and 1.5 mmol m⁻³ based on values found in the literature, respectively, but increased both concentrations appropriately by considering the nutrient discharge in organic and/or particulate forms (Duan et al., 2008; Meybeck, 1982). We understand that these parameters are spatially and temporally variable, and they are connected by biogeochemical processes (parameters), which we still have very limited knowledge. In the current study, we have conducted rigorously numerical experiments to examine these parameters through repeated optimization with observed data, such that they can best represent the observed biogeochemical distribution and variation in the SCS.

The initial nutrient fields and biological parameters came from several sources. We merged the initial NO₃ and PO₄ fields from field observations made in the shelf region in winter 2009 as part of the CHOICE-C project (Carbon Cycling in China Seas-budget, controls and ocean acidification) with data from WOA01 (World Ocean Atlas 2001) in the deep basin. The initial chlorophyll field was from the WOA01 annual average. The initial fields of phytoplankton and detritus, which are not available from field observations or the WOA database, were calculated from chlorophyll data assuming a chlorophyll-to-phytoplankton ratio of 1.59 mg:mmol and a detritus-to-phytoplankton ratio of 0.70 mmol:mmol (Gan et al., 2014). We computed the initial zooplankton from phytoplankton by assuming a zooplankton-to-phytoplankton ratio of 0.1 mmol:mmol. We obtained the boundary values for the biological variables from WOA01 where NO₃ and PO₄ were from

seasonal data for the upper 500 m and from annual data for water columns deeper than 500 m. We spun up the model for 50 years and used results based on the averages of model outputs over the last five years for our analyses.

2.2. Observational data

We validated the model with observed field data and remotely sensed data derived from MODIS (Moderate Resolution Imaging Spectroradiometer, averaged from 2002 to 2012) and SeaWiFS (Sea-viewing Wide Field-of-view Sensor, averaged from 1997 to 2010). The field data (salinity, temperature, NO₃, and PO₄) were collected from four cruises under the CHOICE-C project that occurred from July to September 2009, from December 2009 to February 2010, from October to December 2010, and from April to June 2011. Most of the sampling stations were north of 18°N; for example, SEATS (South East Asia Time-Series Station) and the LU60 station (Fig. 1). We derived the field data of the Kuroshio Edge Exchange Processes (KEEP) from the Joint Global Ocean Flux Study (JGOFS) North Pacific Process Study (NPPS) data set. Most of the stations from KEEP were south of 18°N (<https://www.nodc.noaa.gov/archive/arc0013/0001873/1.1/data/1-data/data/csv/Taiwan/>). Discrete NO₃ and PO₄ samples were collected using a Rosette sampler with GO-FLO bottles (General Oceanics Co.) and were determined colorimetrically using a flow injection analyzer (Tri-223 autoanalyzer).

The remotely sensed chlorophyll represents the mean chlorophyll concentration at penetration depth (Gordon and McCluney, 1975; Morel and Berthon, 1989; Smith, 1981). The penetration depth accessible to remote sensing is (Z_{pd}) = euphotic depth (Z_{eu}) / 4.6 (Morel and Berthon, 1989). Z_{eu} in the SCS basin (isobaths \geq 200 m) is \sim 85 m in winter and \sim 110 m at other times. For the shelf region, researchers estimated an annual mean Z_{eu} of \sim 50 m (Shang et al., 2011). The penetration depth of the blue to blue-green portion of the solar spectrum, which is absorbed most efficiently by phytoplankton, is \sim 20% greater than the penetration depth of Photosynthetically Active Radiation (PAR) (the commonly used euphotic zone depth) in the SCS (Lee et al., 2013). Therefore, for the SCS basin, the remotely sensed chlorophyll represents the mean value in the upper \sim 22 m of the water column in

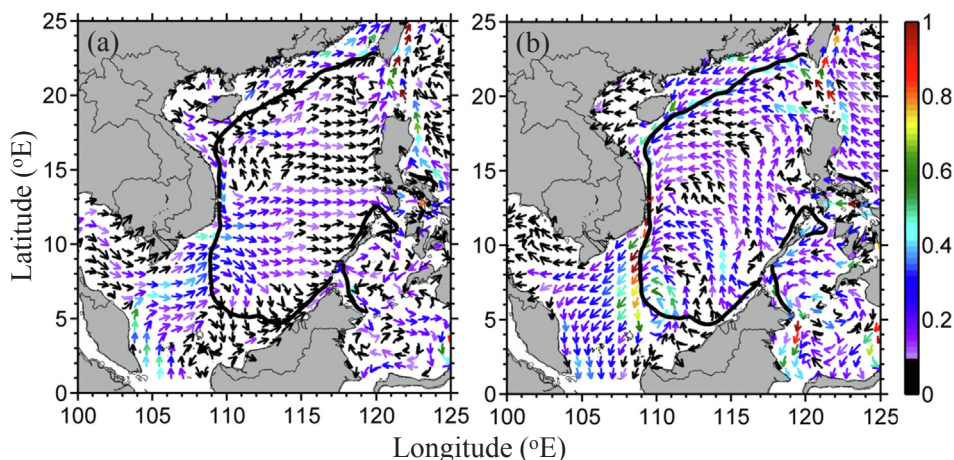


Fig. 3. Model-simulated horizontal mean surface velocity vectors (m s^{-1}) in (a) summer (Jun. - Aug.) and (b) winter (Dec. - Feb.).

winter and the mean value in the upper ~ 29 m at other times. For the shelf region, the remotely sensed chlorophyll represents the mean value in the upper ~ 12 m on average throughout the year.

3. Results

3.1. Hydrography and circulation

The circulation in the upper layer is cyclonic in winter. In summer, the circulation is cyclonic in the northern basin and anticyclonic in the southern basin. The seasonal circulation is shown by the surface velocity vectors in Fig. 3 (also see stream functions in Fig. 1 in Gan et al., 2016b). The ocean circulation in the SCS mainly consists of the wind-driven coastal current over the shallow shelf and basin circulation forced by monsoonal wind stress and inflow/outflow through the straits (Gan et al., 2016a; Qu, 2000). Below the surface layer, the circulation is anticyclonic for the entire year due mainly to the outflow through LS. In the deep layer, a cyclonic circulation prevails during summer and winter and is closely related to the deep intrusion through LS. The results of the distinct cyclonic-anticyclonic-cyclonic (CAC) three-layer circulation in the SCS were validated by geostrophic currents derived from hydrographic data, and its correlation with the inflow-outflow-inflow sandwich-structure transport in LS was recently revealed by Gan et al. (2016a,b). The overall similarities of the physical field between model results and observations provides a reliable physical platform for us to conduct further biogeochemical analysis.

3.2. Chlorophyll in the SCS

Jointly modulated by monsoon wind-induced mixing, river discharge and locally/remotely controlled basin circulation, the horizontal distribution of surface chlorophyll exhibited significant spatiotemporal variabilities. Fig. 4 shows the horizontal distribution of modeled and observed sea surface chlorophyll and its variation over time.

3.2.1. Shelf

In summer, there were high chlorophyll bands near the northern and western coasts, where the Pearl River and the Mekong River discharge into the SCS (Fig. 4a). The river discharges and the associated terrestrial nutrient input in summer stimulate phytoplankton growth in these regions (Dai et al., 2008; Gan et al., 2010). In addition, the upwelling induced by the southwesterly monsoon near the northern and western parts of the SCS (Gan and Qu, 2008; Gan et al., 2009a) provides an additional nutrient source for a biological bloom (Fig. 4a).

However, in winter, the river discharge is lower (accounting for $\sim 6\%$ of the total annual discharge (Dai and Trenberth, 2002)), and

the plume generally flows southwestward under a northeasterly monsoon. Although the total amount of nutrient input in winter from the rivers around the SCS is low due to the lower river discharge, the China Coastal Current (CCC) carries nutrients discharged from the Changjiang River southward along the coast of the ECS, through TS, and towards the broad northern SCS (NSCS) shelf. This input refuels biological production in the entire coastal water off China (Chen, 2008; Han et al., 2013) which is shown in the right column of Fig. 4a.

Fig. 4b shows that the chlorophyll level had twin peaks in the northern and southern parts of the SCS shelf during summer and winter. The overall concentration in the southern part was lower than in the northern part, mainly because of the lack of a massive nutrient input from river discharge. Note that diffuse sources of nutrients (such as agriculture, sewage discharge, small runoffs) along the coast and benthic processes were not included in the model, which might explain some of the disagreement between the model output and the field observations in coastal areas and shallow waters, for example, the high chlorophyll level along the Northern Borneo coast, in the Beibu Gulf (northwest of Hainan Island), and in the Gulf of Thailand (Fig. 4a). In addition, the high loading of inorganic suspended matter and colored dissolved organic matter (CDOM) in coastal waters could cause remotely sensed data to be significantly overestimated (Ruddick et al., 2001). This is also why the model output agreed better with the satellite data with regards to a seasonal trend, but had relatively low magnitudes (Fig. 4b).

3.2.2. Basin

Water column stratification is strongest during summer. Nutrients in the surface layer were nearly depleted because the upward advection of deep water was blocked by the stable pycnocline (Wu et al., 2003). Therefore, the chlorophyll level in the basin was lowest during summer.

In winter, when there is a strong northeast monsoon, the vertical mixing in the upper water column is strongest. At this time, the mixed layer depth (MLD) can exceed 80 m, whereas it is merely ~ 20 m during other seasons (Qu, 2001). Subsurface water is an important nutrient source for the surface water so that the chlorophyll level is highest in winter. Several local physical processes also enhance local upwelling to further enrich the nutrients in the surface layer. The most prominent processes are the strong upwelling induced by the seasonal cyclonic eddy northwest of Luzon (Shaw et al., 1996) and the cyclonic eddy generated by the recirculation of the jet separation southeastern of Vietnam (Gan and Qu, 2008). Our model captured these seasonal cyclonic eddies well in the three dimensional circulation (Gan et al., 2016a) and in the strengthened phytoplankton blooms (Fig. 4a).

The seasonality of the chlorophyll is seen clearly in the time series of the domain-averaged surface chlorophyll levels of the model output and

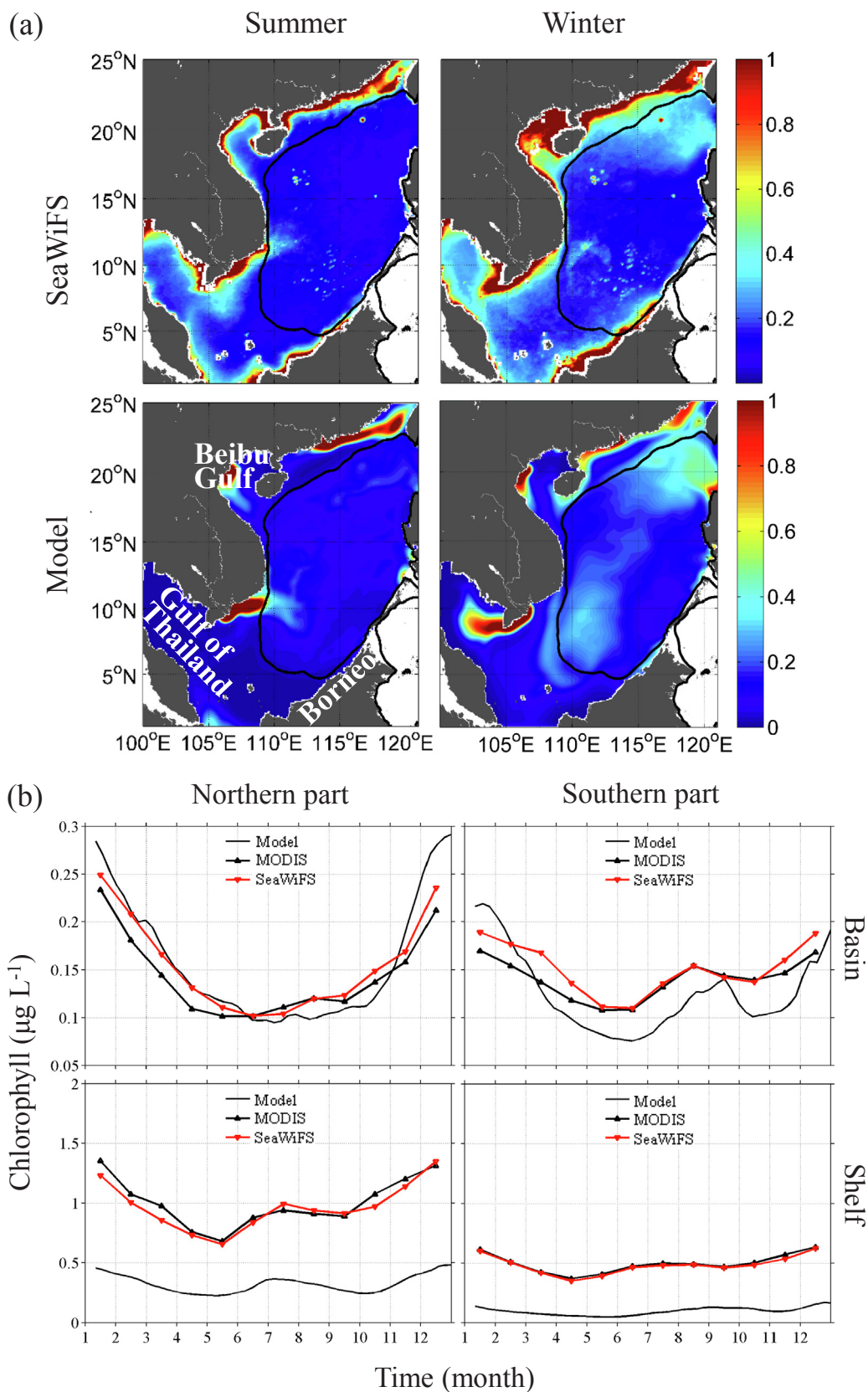


Fig. 4. (a) Distributions of sea surface chlorophyll *a* ($\mu\text{g L}^{-1}$) in summer and winter from SeaWiFS satellite data (upper panel) and the model (lower panel). (b) Seasonal variations in domain-averaged surface chlorophyll from the model and satellite remote sensing data. The upper panel in (b) is the SCS basin (> 200 m water depth) and the lower panel is the SCS shelf (≤ 100 m water depth). The left column is the northern part of the SCS (north of 15°N), and the right column is the southern part of the SCS (south of 15°N).

field observations. The model reproduced the observations closely in magnitude and phase. The chlorophyll concentration stayed low, ranging from $\sim 0.1 \mu\text{g L}^{-1}$ (summer) to $\sim 0.25 \mu\text{g L}^{-1}$ (winter) in the north and south (Fig. 4b), reflecting the oligotrophy in this area. The seasonal trend was smooth in the north. The high chlorophyll level induced by the Pearl River plume and the coastal upwelling off southern China did not appear to be transported out of the shelf region. However, in the southern part of the SCS, besides the high chlorophyll level in winter, there was also a weak peak in summer which we attribute to the cross-slope propagation of the Mekong River plume and the coastal upwelling off eastern Vietnam.

The spatiotemporal characteristics in the model results and in the observations shown in Fig. 4 agreed with our general understanding of seasonal variation of the biological processes in the SCS. However, the influence of the dominant three-dimensional CAC circulation and associated inflow/outflow on the nutrient flux and biological productivity in the SCS has not been assessed. In addition, the links between nutrient distribution and transport remain largely unknown; the connections between nutrient dynamics and biological response are not clear. This study aims to fill these knowledge gaps.

3.3. Nutrient distribution

We compared the nutrient distributions produced by the model and

the observed distributions. The distributions shown in Fig. 5 are from meridional and zonal sections across the entire SCS. Because the SCS is an oligotrophic sea, the nutrient concentration in the surface layer was almost undetectable in most areas. The nutrient concentration increased rapidly downward with depth in the upper ~ 1000 m, and then the concentration remained relatively stable in the deeper layer. There was a higher nutrient concentration around 2000 m depth and a slightly lower concentration in the bottom layer, but the range of variation did not exceed $\pm 5\%$ of the mean value below 1000 m. The model results compared reasonably well with the field observations along the two sections shown in Fig. 5.

In Fig. 6, we compare model results and observations at all the sampling stations. The model results and observed data deviated more from a 1:1 line in the upper layer where biogeochemical activities were relative strong. The model results were systematically slightly lower than the observations. There are many reasons for the differences between the model results and the observations; nevertheless, the overall good linearity between the two demonstrates that the model reproduced the observed features in the SCS.

3.4. The vertical structures in the SCS and WPO

The SCS water originates from the WPO through LS (Gan et al., 2016a; Wong et al., 2007b). However, the vertical distributions of

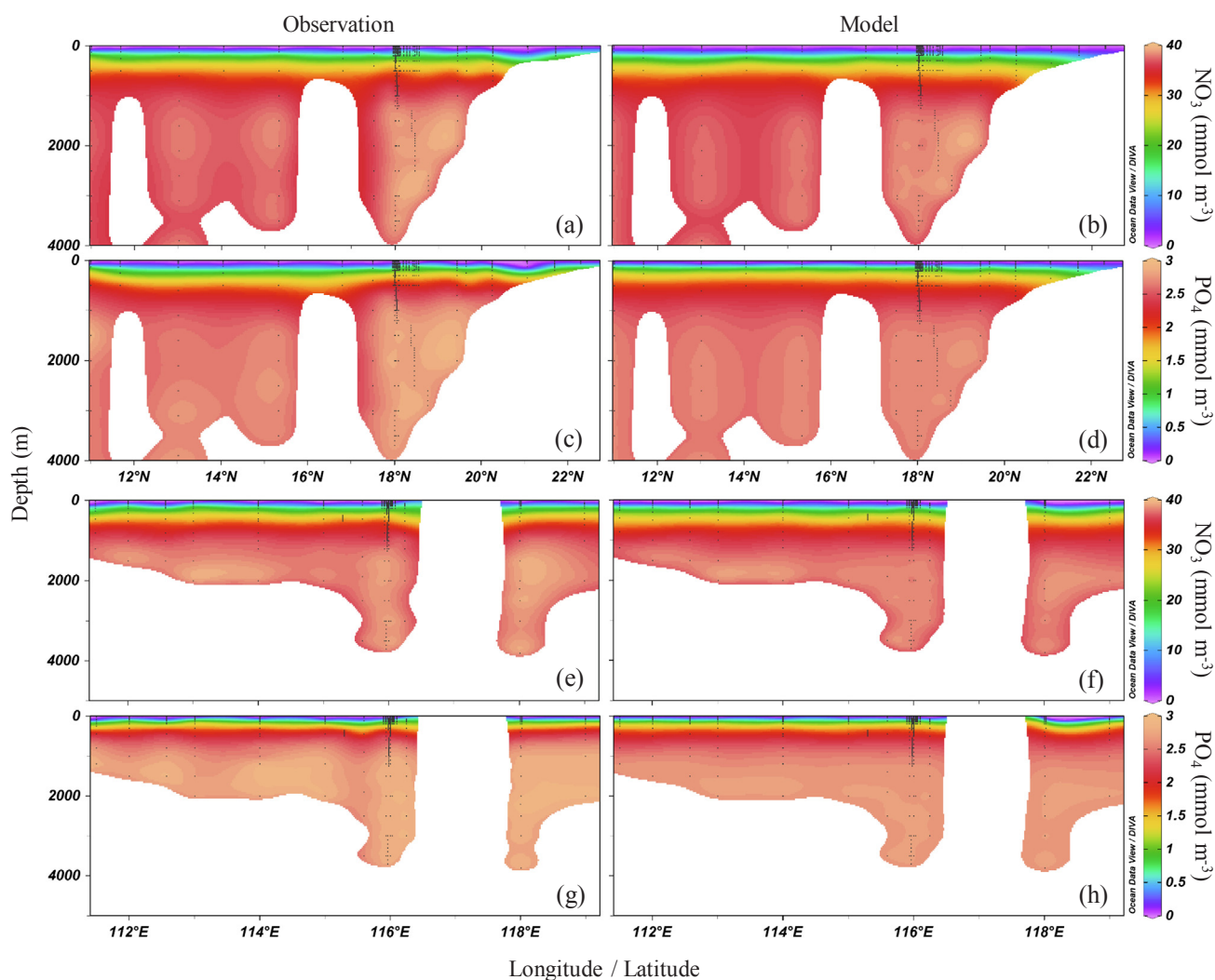


Fig. 5. NO_3 and PO_4 distributions at meridional (a - d) and zonal (e - h) sections (see Fig. 1 for location) for observed data and model result. The black dots represent sampling points.

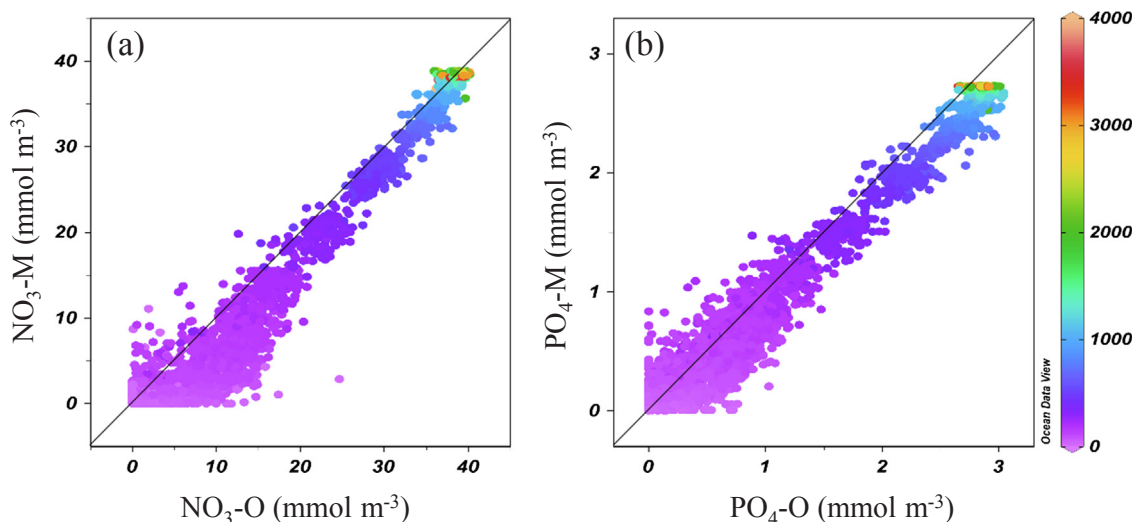


Fig. 6. Comparison between model (M) and observation (O) for NO_3 and PO_4 . Each point in the scatter charts represents an observation-model pair (all the observational stations from various cruises are shown in Fig. 1). The color of the points represents the sampling depth of each data point.

physical and biochemical parameters have been found to be very different between these two bodies of water (Chiang et al., 2018; Du et al., 2013; Gong et al., 1992). Researchers have yet to explain these differences.

Fig. 7 shows the vertical profiles of salinity, temperature, NO_3 and PO_4 at SEATS and LU60. SEATS represented the SCS water, and LU60 represented WPO water (Fig. 1). All variables differed significantly between SEATS and LU60, especially in the upper 1000 m. The salinity exhibited similar patterns at the two locations (Fig. 7a): it increased sharply from a low value in the surface to a maximum at ~ 150 m, then minimized ~ 500 m, before it steadily increased again in the deeper layer. However, the vertical distribution of salinity at SEATS was more uniform than that at LU60, except for the very low surface value at SEATS due to the terrestrial freshwater discharge around the SCS (Wyrski, 1961).

The sea surface temperature (SST) at the two sites were very similar. The similarity suggests similar atmospheric thermal forcing and heat transport (Gan et al., 2016a). However, the temperature dropped more quickly at SEATS immediately below the surface layer. The difference in temperature between the two sites continued to expand with depth until it reached a maximum of ~ 5 °C between ~ 300 and ~ 400 m. Below 400 m, the temperature difference narrowed and merged at ~ 900 m and below 900 m (Fig. 7b).

On the contrary, the nutrient concentration at SEATS was considerably higher than that at LU60 in the upper ~ 900 m, except in the surface mixed layer where the nutrient concentration was extremely low for both stations due to biological consumption (Fig. 7c, d). The maximum differences were as high as 12 and 0.8 mmol m^{-3} for NO_3 and PO_4 , respectively, at ~ 350 m. The model simulation captured there vertical characteristics of physical and biogeochemical properties very well.

The model-observation comparisons (Figs. 5, 6, and 7) provided good data to validate the model. However, the nutrient patterns along these sections and stations were not enough to depict the full picture of the nutrient distribution in the SCS. We had to use the model results to dynamically interpolate and extrapolate the three dimensional distributions of the nutrients, and discuss the distributions' control mechanisms.

4. Discussion

4.1. Implication from the nutrient vertical structure

The nutrient distribution is intrinsically modulated by the physical and biological processes inside the water mass and extrinsically determined by the origin of water. Huge freshwater discharge contributes to lower salinity in the surface layer (Fig. 7a) and brings large amounts of nutrients (Chen et al., 2001). The nutrient contribution from river discharge can be roughly estimated based on the water residence time. Under the assumption that water in the upper layer of the SCS was from the WPO, and that river discharge was the only external nutrient source, the water residence time (τ) can be estimated as follows:

$$\tau = \frac{([N]_{SCS} - [N]_{WPO})V}{([N]_R - [N]_{WPO})F} \quad (1)$$

where $[N]_{SCS}$, $[N]_{WPO}$ and $[N]_R$ are the average nutrient concentrations in the upper layer of the SCS, the upper layer of the WPO and river discharge, respectively. V is the volume of water in the upper layer of the SCS, and F is the flow rate of rivers.

To compensate for the nutrient deficit due to the dilution by intruding WPO water, a residence time of ~ 101 years would be needed for NO_3 if we ignored sinking due to biological metabolism. Our estimated residence time based on river input only was much longer than the actual residence time of ~ 3 years (Liu and Gan, 2017) which suggested that the N contribution from river input was minor compared to the nutrient enrichment by physical transport in the upper layer.

The PO_4 concentration in river discharge was lower than the mean value in the upper layer ($\sim 1.55 \text{ mmol m}^{-3}$). Therefore, other sources must have been responsible for the PO_4 input. Enhanced vertical mixing might also result in a higher nutrient concentration in the upper layer. However, there is evidence that suggests that mixing alone cannot account for all the nutrients in the upper layer (e.g. Gong et al., 1992). Considering the characteristics of the active CAC circulation in the SCS, and the associated inflow/outflow through the straits surrounding the sea, the lateral and upward advective flux of deep water might be the main source of nutrients in the upper layer (also see Section 4.3.).

4.2. Total nutrient transport

Nutrient transport and budget have long been analyzed based on dissolved inorganic forms, while the organic nutrient pool has been ignored by assuming that the main fraction of organic matters is

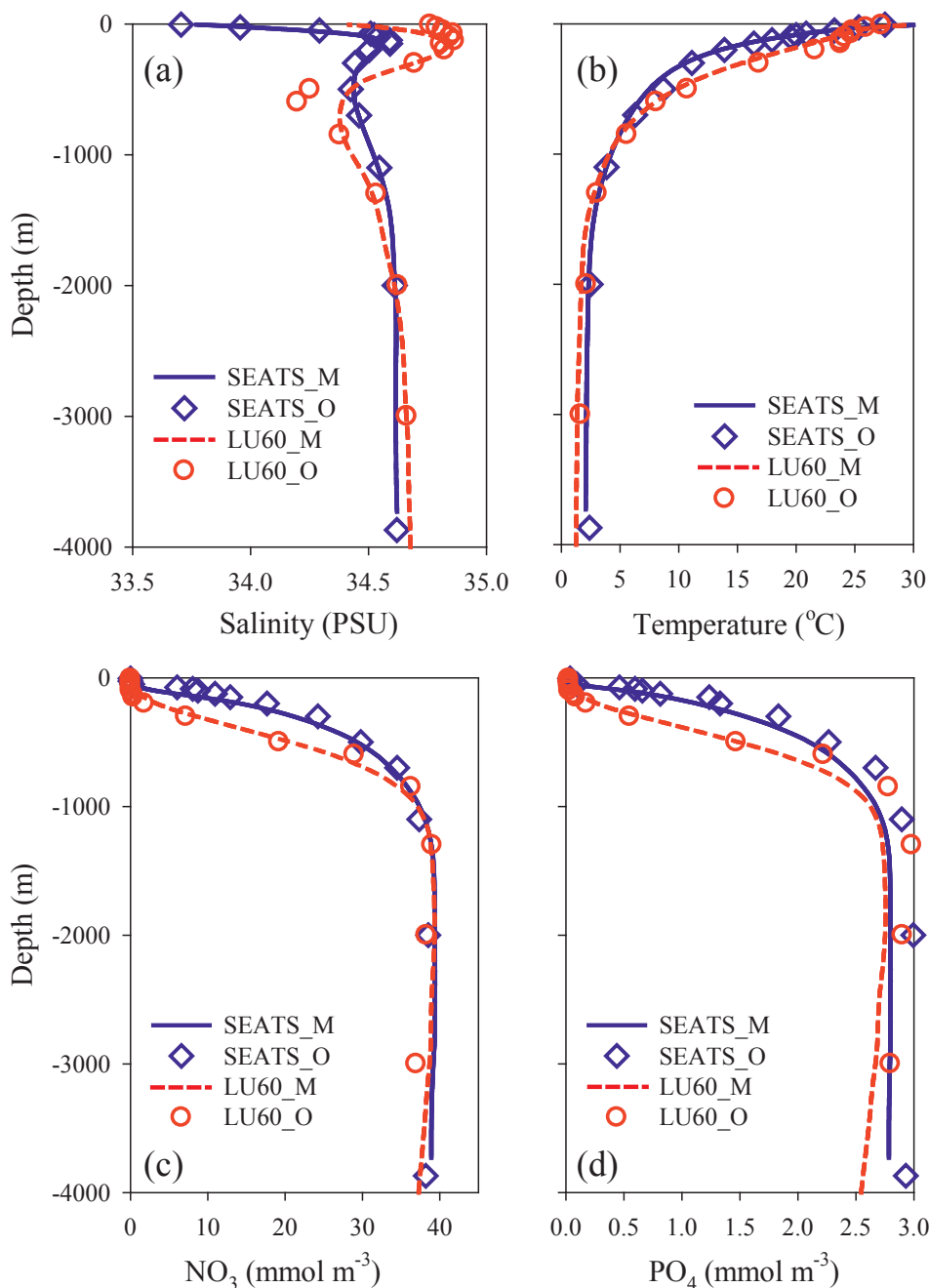


Fig. 7. Vertical profiles of (a) salinity, (b) temperature, (c) NO_3 and (d) PO_4 from model results (M) and field observations (O) at SEATS and the LU60 station during a cruise in May 2011. Blue solid lines represent model results at SEATS. Blue open diamonds represent observations at SEATS. Red dashed lines represent model results at LU60. Red open circles represent observations at LU60. (For interpretation of the references to color in this figure legend, the reader is referred to the web version of this article.)

refractory (Ogawa and Tanoue, 2003). This assumption is valid in the open ocean, but might be violated in highly productive shallow waters where labile organic nutrients, comprising marine organisms and their metabolites, might be present at higher levels than inorganic nutrients (Liu et al., 2010b; Santos et al., 2008; Zuo et al., 2016). These autochthonous organic nutrients are produced through consumption of dissolved inorganic nutrients and return to the inorganic pool quickly through remineralization as shown by Eqs. (A1) to (A3):

The proportion of organic and inorganic forms varied spatially. Fig. 8 shows the proportion of dissolved inorganic nitrogen (DIN, represented by NO_3 and NH_4 in the model) and particulate organic nitrogen (PON, represented by phytoplankton, zooplankton, and detritus in the model) along the central axis of the Pearl River plume during

summer. The proportion of DIN and PON varied dramatically with the northeastward propagation of the river plume. DIN dominated the nitrogen pool in the near field of the plume, but decreased sharply in the middle and far field due to biological consumption. Most of the DIN is converted to organic forms and represented over 80% of the total nitrogen pool. These labile organic nutrients have a very short turnover time and drive the biogeochemical cycling in the water column. Therefore, ignoring the organic forms could lead to considerably underestimating the nutrient flux.

To evaluate how much labile organic forms contribute to nutrient transportation, we calculated total nitrogen (TN) fluxes through the four major straits around the SCS by summing all DIN and PON. Fig. 9 compares the TN flux and the DIN flux through different channels. The

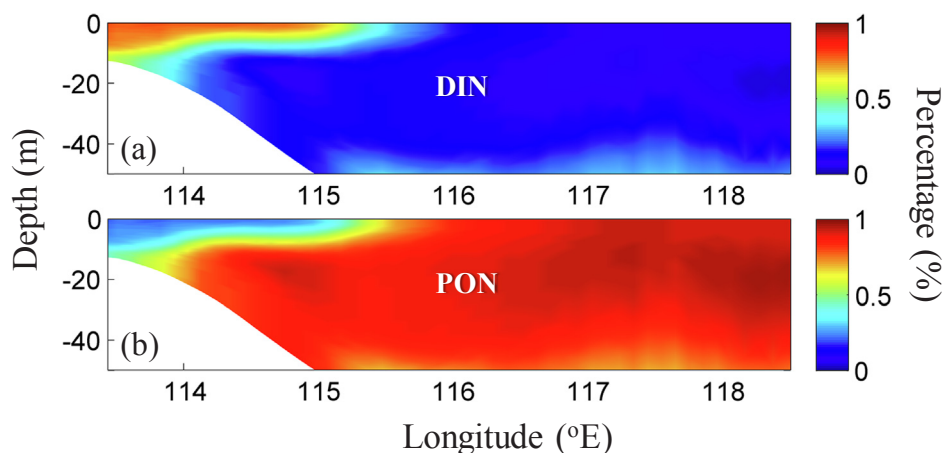


Fig. 8. Vertical distribution of the ratio of (a) DIN and (b) PON to the total nitrogen pool along the axis of the Pearl River plume (22.1°N) in summer.

difference between the two fluxes was small for LS (Fig. 9a) because the DIN flux below the nutricline dominated the total water column-integrated nitrogen transport. The contribution from the organic forms in the euphotic layer was trivial compared to the strong DIN flux in the deeper layer. However, for the other three shallower straits, nitrogen transport in terms of DIN or TN was very different. The difference in the DIN and TN fluxes was visible in MS (Fig. 9b), but this difference was not as large as in the other two straits. The annually averaged DIN flux was low (-0.13×10^6 mmol s^{-1} , outflux) in KS and quite stable throughout the year, while the annually averaged TN flux was about 6 times higher (-0.88×10^6 mmol s^{-1} , outflux) and exhibited significant seasonality (Fig. 9c). The contrast was even stronger for TS. Through TS, the annually averaged DIN flux was very weak (0.09×10^6 mmol s^{-1}) and traveled mainly from the ECS to the SCS (influx); however, the annually averaged TN flux was over 20 times stronger (-2.06×10^6

mmol s^{-1}) and traveled in the opposite direction (outflux), due to the northward transport that increased after winter and peaked in summer (Fig. 9d). It is commonly considered that the level of dissolved inorganic nutrients carried by the southward CCC in winter was much higher than the total amount of northward transport in other seasons (Chen, 2008). By considering the nutrients in labile organic forms, TN transport is an outflux from the SCS. To understand the ecosystem dynamics in the entire SCS, TN rather than DIN flux needs to be considered.

Like the nitrogen transport, huge differences also exist between dissolved inorganic phosphorus (DIP) and total phosphorus (TP), although the differences were not as significant as those between DIN and TN. The smaller differences between DIP and TP is not surprising because the remineralization rate of organic phosphorus is much higher than that of nitrogen (Hopkinson et al., 2002). The annually averaged

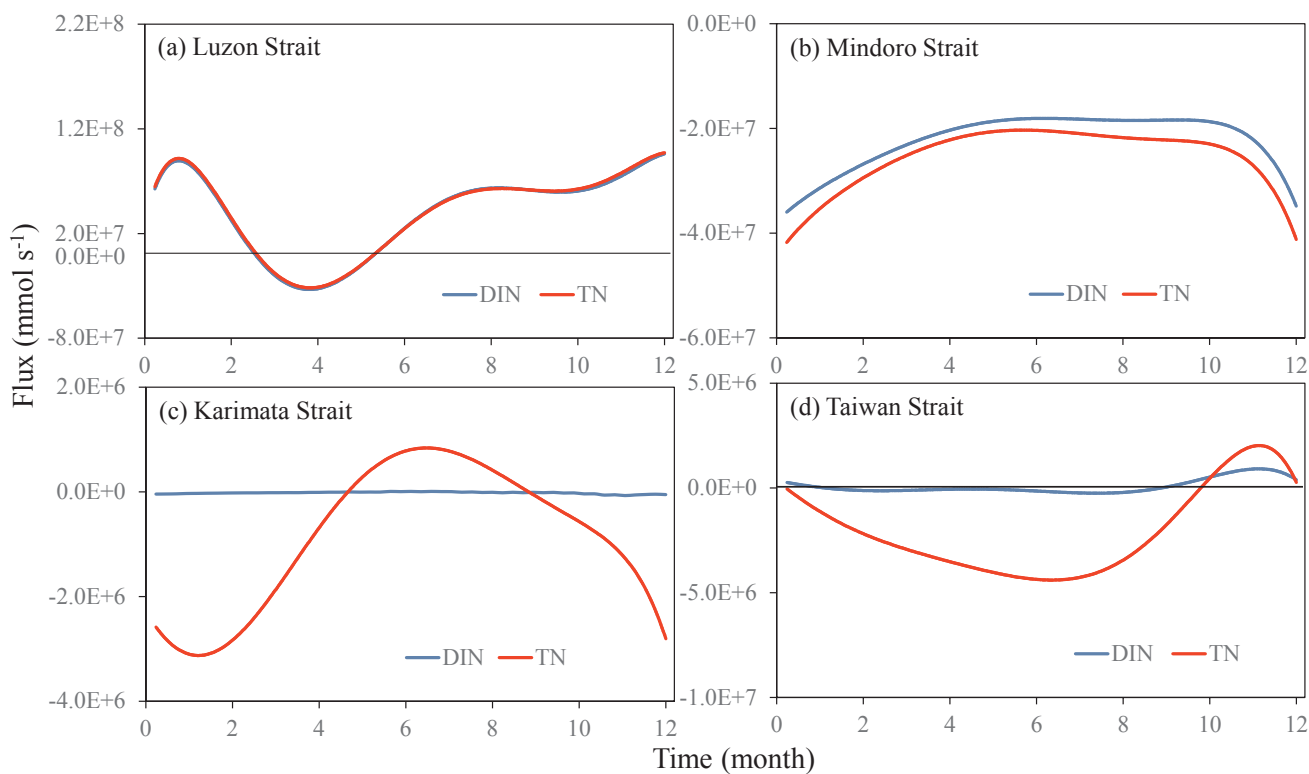


Fig. 9. Time series of depth-integrated DIN (blue solid line) and TN (red solid line) flux (mmol s^{-1}) through (a) Luzon Strait, (b) Mindoro and Balabac Strait, (c) Karimata Strait, and (d) Taiwan Strait. Positive and negative values represent nutrient flux into and out of the SCS, respectively. (For interpretation of the references to color in this figure legend, the reader is referred to the web version of this article.)

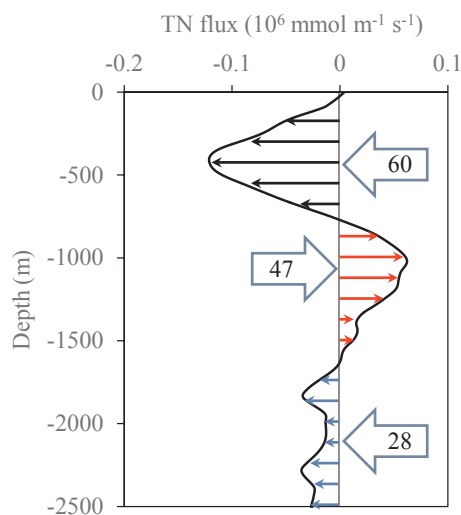


Fig. 10. Annual mean vertical profile of TN transport through Luzon Strait. Negative and positive values represent the westward and eastward transport, respectively. The number inside the arrows represents the layer-integrated transport in units of 10^6 mmol s^{-1} .

DIP fluxes through TS and KS were -0.06 and $-0.07 \times 10^6 \text{ mmol s}^{-1}$, respectively, but the annually averaged TP transport reached a much higher $-0.20 \text{ mmol s}^{-1}$ in the former and $-0.12 \times 10^6 \text{ mmol s}^{-1}$ in the latter. The result demonstrates the importance of including organic nutrients when calculating transport and estimating the nutrient budgets in the SCS.

4.3. Layered transport through the LS and 3D nutrient structure of the SCS

Based on the CAC three-layer circulation in the SCS and the corresponding inflow-outflow-inflow transport in LS (Gan et al., 2016a), we divided the nutrient transport through LS into the three layers following the direction of volume transport. The vertical variability of the nutrient transport resembled the variability of the volume transport, but had unique features which the TN flux in Fig. 10 shows. The strongest volume inflow occurred in the surface layer, while the nutrient influx peaked in the subsurface layer near 500 m due to the oligotrophic nature of the SCS characterized by the nutrient-deplete surface layer. The strongest nutrient influx still occurred through the upper layer ($60 \times 10^6 \text{ mmol s}^{-1}$) due to the strong volume transport. Nevertheless, the nutrient concentration was high ($28 \times 10^6 \text{ mmol s}^{-1}$) in the deep layer which made this layer another important source of nutrients for the SCS despite its volume transport being relatively low. After compensating for the outflow through other straits in the upper layer (Fig. 9), a downward flux from the upper layer and an upward flux from the deep layer would be expected to form an outflow through LS in the middle layer (Gan et al., 2016b) ($-47 \times 10^6 \text{ mmol s}^{-1}$). If we summed the fluxes in all the layers, the net TN influx through LS would be $41 \times 10^6 \text{ mmol s}^{-1}$. Such an inflow-outflow-inflow vertical structure of nutrient transport through LS not only recasts the vertical profile, but also shapes the layered horizontal distribution of nutrients in the SCS.

Fig. 11a shows the vertical profile of the annual mean domain-averaged NO_3 of the SCS and compares it with the same profile in LS. In the upper layer, the nutrient concentration was lower in LS than in the SCS. With the strong volume inflow, we estimated a deficit of $\sim 18 \times 10^6 \text{ mmol s}^{-1}$ in TN in the upper layer because of intruding WPO water that has a low nutrient concentration. As we discussed in section 4.1, river input and vertical mixing are far from being enough to compensate for the deficit. The only compensating source, therefore, would be the deep intrusive transport ($\sim 28 \times 10^6 \text{ mmol s}^{-1}$ in TN, Fig. 10), and ensuing upward transport. When the deep water with high nutrient loading advects upward and combines with the sinking upper-

layer water to form the middle layer water, some water masses from the deep layer reach the upper layer because of locally forced processes such as topography, eddies, and waves before they leave the SCS through the LS (Gan et al., 2016a; Liu and Gan, 2017). Modulated by this kind of basin-scale three-dimensional circulation, part of the nutrients from the deep layer can be advected to the upper layer.

Under the extrinsic control of the sandwich-like transport through LS, the water exchange through other straits, and the intrinsic modulation by interior vertically variable circulation (Gan et al., 2016b), the three-dimensional distribution of nutrients in the SCS exhibited a unique layered horizontal distribution of NO_3 in the upper, middle, and deep layers which is shown in Fig. 11b.

We used feature scaling ($x' = \frac{x - \min(x)}{\max(x) - \min(x)}$, where x represents the original nutrient data array, x' represents the unified nutrient data array, and \min and \max represent minimum and maximum values) to unify and magnify spatial differences and highlight the horizontal structures in different layers. Fig. 11b shows that an increasing north-east to southwest nutrient gradient was in the 500 m layer, reflecting the strong Kuroshio intrusion through LS. Because in upper layer, the nitrate concentration of the Kuroshio was much lower than that of the SCS (Fig. 5c, d), the strong intrusion diluted the nitrate concentration in the upper layer of the SCS. In the middle layer, the sinking upper layer water that had low nutrient concentration met the rising deep water that had a high nutrient concentration in the south basin. The upward advection from the deep layer also joined the water in the middle layer directly during the outflow, especially in the northern basin (Liu and Gan, 2017). A cyclonic circulation dominates the intrusive deep water (Gan et al., 2016b). This deep water has a high nutrient loading and flows southwestward along the slope. At the same time, a strong subduction of water in the middle layer occurred over the eastern slope and an obduction occurred over the western slope of the south basin (Liu and Gan, 2017), forming a decreasing northwest to southeast gradient in the deep layer of the SCS.

4.4. Nutrient exchange with adjacent seas

The nutrient exchange with the adjacent seas is largely modulated by volume transport. This exchange is also strongly shaped by the uneven spatiotemporal distribution of nutrients. The time series of the TN fluxes between the SCS and the adjacent seas are presented in Fig. 12. All these time series showed significant seasonal and spatial variability. The westward upper-layer intrusion through LS was the strongest during winter as it benefits from the weakened Kuroshio current (Qu, 2000). The eastward transport in the middle layer was the strongest in winter and early spring to balance the transport in the upper layer. However, the westward nutrient intrusion in the deep layer was stronger in late summer and early autumn which was intrinsically associated with the stronger cyclonic circulation in the deep SCS basin at this time (Gan et al., 2016b). Therefore, unlike the U-shaped seasonal variation (increasing from a minimum in middle of the year) in the depth-integrated volume transport through LS (Fig. 14 in Gan et al., 2016a), the depth-integrated nutrient transport through LS had a double-peak seasonal trend (Fig. 9a). This reflects the strongest westward intrusion in the upper layer where the intrusive velocity was strongest during winter, and in the deep layer where the cyclonic circulation was strongest during late summer and early autumn.

The eastward nutrient transport through MS in the upper 400 m, which forms the main outflow of the upper-layer waters in the SCS, was also stronger in winter and weaker in summer (Figs. 9b and 12b). There was a westward inflow at ~ 500 m, but it was much weaker and varied less with the season (Fig. 12b). Nutrient exchanges through the other two straits (TS and KS) were one to two orders of magnitude lower due to the shallow water and low nutrient concentrations (Fig. 9c, d and Fig. 12c, d). Different from the other straits, the nutrient transport through TS was stronger in summer and weaker in winter under the

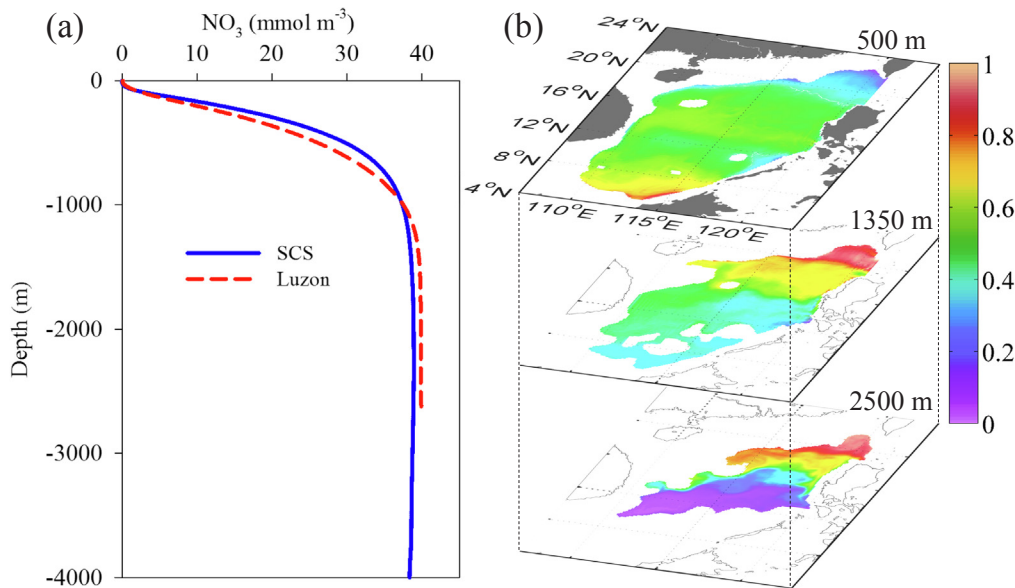


Fig. 11. Vertical profiles of (a) annual mean domain-averaged NO_3 in the SCS and annual mean section-averaged NO_3 across LS, and (b) annual mean layered NO_3 horizontal distribution. The horizontal data were standardized using the feature-scaling method (Section 4.3) to unify the scale and highlight the spatial variation.

influence of the Pearl River discharge (Figs. 9d and 12d).

4.5. Nutrient dynamics in the SCS

Biological activities that responds to and superimpose on the three-dimensional ocean circulation are the major controllers of nutrients in the upper ocean. Assimilation and remineralization transform nutrients from one form to another and regulate their downward transport. These processes intensify the spatial gradients and, in turn, strengthen the diffusion. A first-order assessment of nutrient dynamics in the upper layer of the SCS can be made by analyzing the term balances in the nutrient equations (Equations A1 - A3) to determine how different factors evolve and their contribution to the variation in nutrients.

When calculating the term balances, we amend the horizontal advection and vertical advection from the sigma surface advection back to geopotential surface advection. The domain averaged horizontal and

vertical advection terms for nutrients over the shelf and basin are shown in Figs. 13–16.

4.5.1. Shelf

Fig. 13a shows the variation in the time series of the NO_3 terms in the upper 10 m of the water column over the SCS shelf. Most of the river plume is confined to this layer (Gan et al., 2009b). Vertical advection dominated the source of NO_3 . The domain average of the vertical advection that peaked during the summer (Fig. 13a) reflected the strong coastal upwelling along the western and northern shelves (Gan and Qu, 2008; Gan et al., 2009a). The northeastward transport of the Pearl River plume from the SCS to the ECS during the summer and the southwestward transport of the CCC from the ECS to the SCS during the winter contributed to the weak negative and positive horizontal advection, respectively, as also found by Chen (2008) and Han et al. (2013).

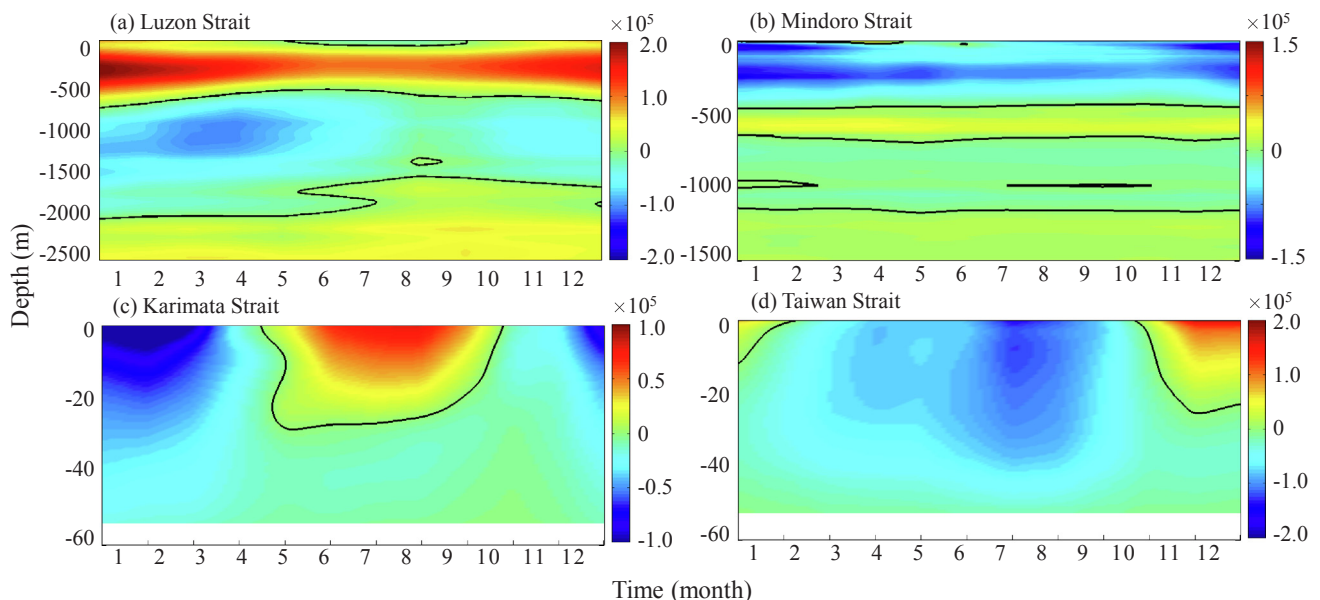


Fig. 12. Time series of vertical profile of TN flux ($\text{mmol m}^{-1} \text{s}^{-1}$) through the (a) Luzon Strait, (b) Mindoro and Balabac Strait, (c) Karimata Strait, and (d) Taiwan Strait. Positive and negative values represent the flow into and out of the SCS, respectively. The black contour lines represent the zero line.

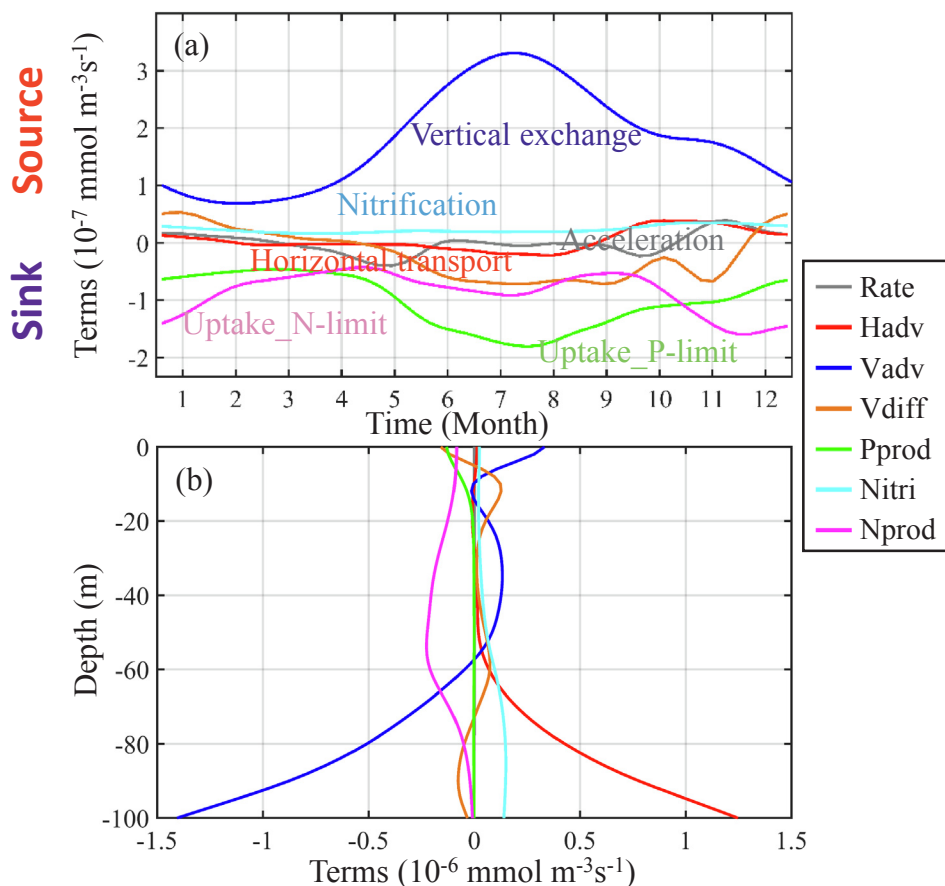


Fig. 13. (a) Time series of volume-averaged terms in the NO_3 equation in the upper 10 m of the SCS shelf (isobath < 200 m). (b) Vertical profiles of annual mean domain-averaged terms for NO_3 on the shelf. All terms were calculated by placing them on the right-hand side of the equation, such that a negative rate means an increasing rate of variation and a positive rate means a decreasing rate of variation. Hadv = horizontal nonlinear advection, Vadv = vertical nonlinear advection, Vidff = vertical diffusion, Pprod = production through PO_4 , Nitri = nitrification, and Nprod = production through NO_3 .

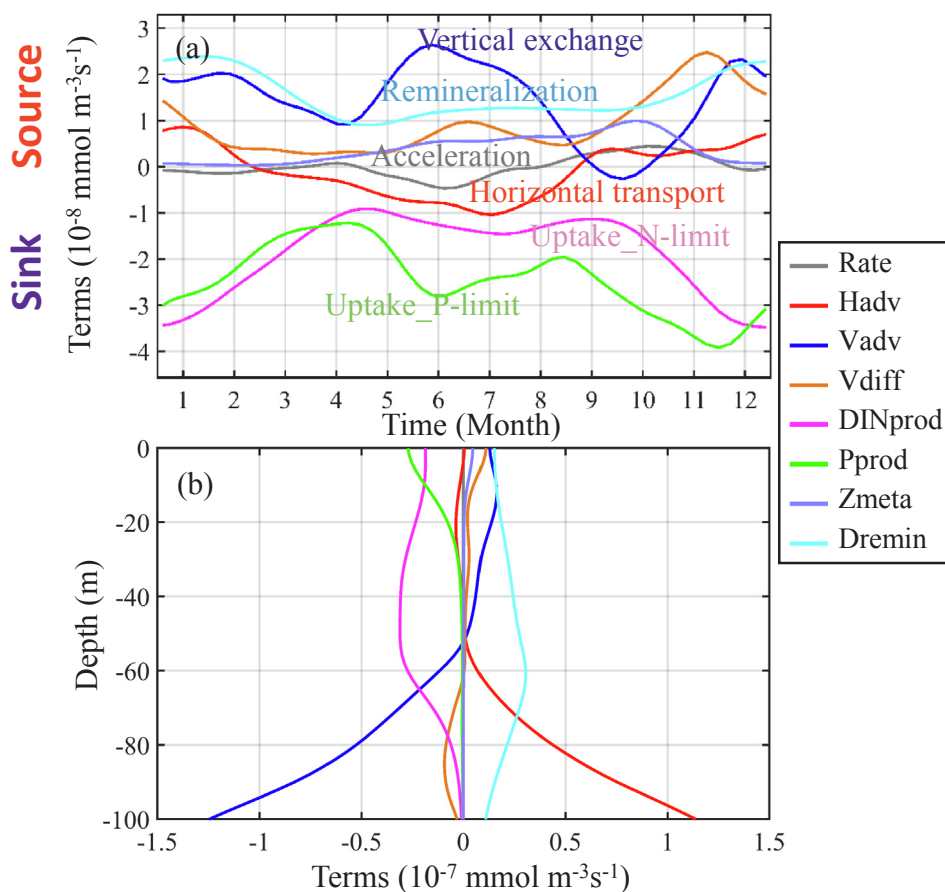


Fig. 14. (a) Time series of volume-averaged terms in the PO_4 equation in the upper 10 m of the SCS shelf (isobath < 200 m). (b) Vertical profiles of annual mean domain-averaged terms for PO_4 on the shelf. Hadv = horizontal nonlinear advection, Vadv = vertical nonlinear advection, Vidff = vertical diffusion, DINprod = production through NO_3 and NH_4 , Pprod = production through PO_4 , Zmeta = zooplankton metabolism and excretion, and Dremmin = detritus remineralization.

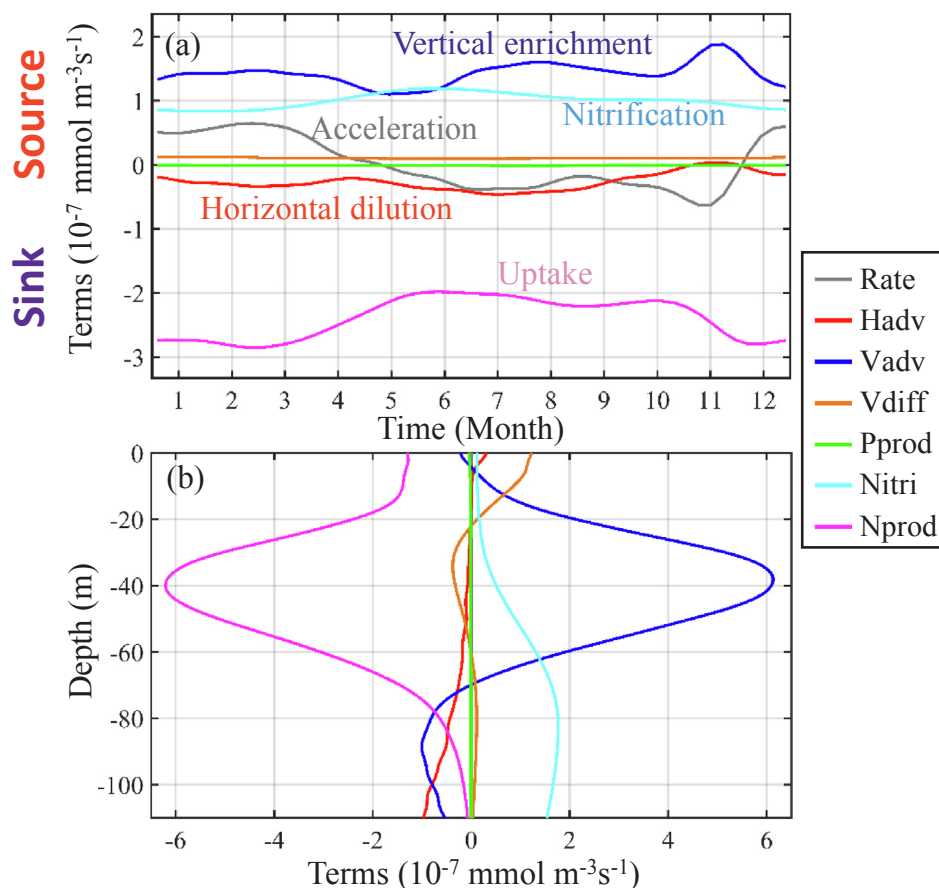


Fig. 15. (a) Time series of volume-averaged terms in the NO_3 equation in the euphotic layer (upper 110 m) of the SCS basin (isobath ≥ 200 m). (b) Vertical profiles of annual mean domain-averaged terms for NO_3 in the basin. The terms are defined in the same way as in Fig. 13.

Biological production is the main sink. The production through PO_4 was significantly higher than the production through NO_3 during summer because of the river discharge which has a very high N:P ratio (Cai et al., 2004). On the contrary, the production through NO_3 was higher than the production through PO_4 during winter when the river discharge was the lowest so that there might have been P-limitation in the river plume and N-limitation in other areas (Gan et al., 2014). A high concentration of NO_3 in the upper layer also caused a downward diffusive flux except during winter when terrestrial NO_3 input was low.

The vertical distribution of the terms demonstrated that the higher production through PO_4 , which results from the high N:P ratio (above 13.3 (Gan et al., 2014)) in riverine water, was confined to the upper ~ 10 m (Fig. 13b). Production through NO_3 took over in the deeper water until it became negligible at the bottom of the euphotic layer. Strong horizontal and vertical advection was the NO_3 source and sink in the subsurface layer ($> \sim 60$ m), respectively, indicating that NO_3 came from the shoreward advection of deep water and was balanced by upward advection during the upwelling which, for example, occurred in the northern SCS shelf (Gan et al., 2009a). Biologically, NO_3 sourced from the nitrification would generally be consumed by phytoplankton production, but the vertical distribution of these two terms were dislocated due to the relatively low remineralization and nitrification rate.

Unlike the NO_3 , we found that remineralization dominated the source terms of PO_4 in the upper ~ 70 m layer. The contribution from vertical advection only exceeded remineralization in the surface layer during summer when coastal upwelling was strong (Fig. 14). This is because that the remineralization rates of organic nitrogen and phosphorus are different in our model (Table 1) in which the remineralization rate of organic phosphorus is much higher than that of

nitrogen (Dyhrman et al., 2007). Vertical diffusion also served as a significant source of PO_4 (Fig. 14a), suggesting a strong downward increasing PO_4 that opposed the vertical distribution of NO_3 in the upper layer. This downward gradient occurred because of the P-depletion in the plume where the N:P ratio could be as high as ~ 200 outside of the estuary (Gan et al., 2014). Like NO_3 , the horizontal transport term of PO_4 reflected the northeastward transport of the Pearl River plume and the southwestward transport of the CCC during summer and winter respectively. Again, the sink term of PO_4 was attributed to biological production, just as it was with NO_3 . Thus, the P-limitation during summer and enhanced vertical mixing in winter could be described by Pprod and DINprod, respectively (Fig. 14a). The balance of PO_4 in the subsurface layer ($> \sim 60$ m) was like the balance of NO_3 except that the dislocation between biological uptake and remineralization was much smaller because of the much higher turnover rate of PO_4 (Fig. 14b).

4.5.2. Basin

The SCS basin is different from the nutrient rich shelf sea in that the basin is typically oligotrophic in surface layer. Fig. 15 shows the volume-averaged terms of NO_3 in the euphotic layer ($Z_{eu} = 110$ m (Shang et al., 2011)) of the SCS basin. The source of NO_3 in the euphotic layer was vertical advection and the decomposition of organic matter (represented by nitrification as shown in Equation A(1)). Although the nitrification in the euphotic ocean has seldom been reported due to methodological difficulties (Xu et al., 2017), it is suggested that the fractional contribution of nitrification to “external” NO_3 could be as high as 19 to 33% (Yool et al., 2007), which generally agrees with the 33% that we calculated in this study. The seasonal variation in nitrification generally followed the seasonal trend of biological

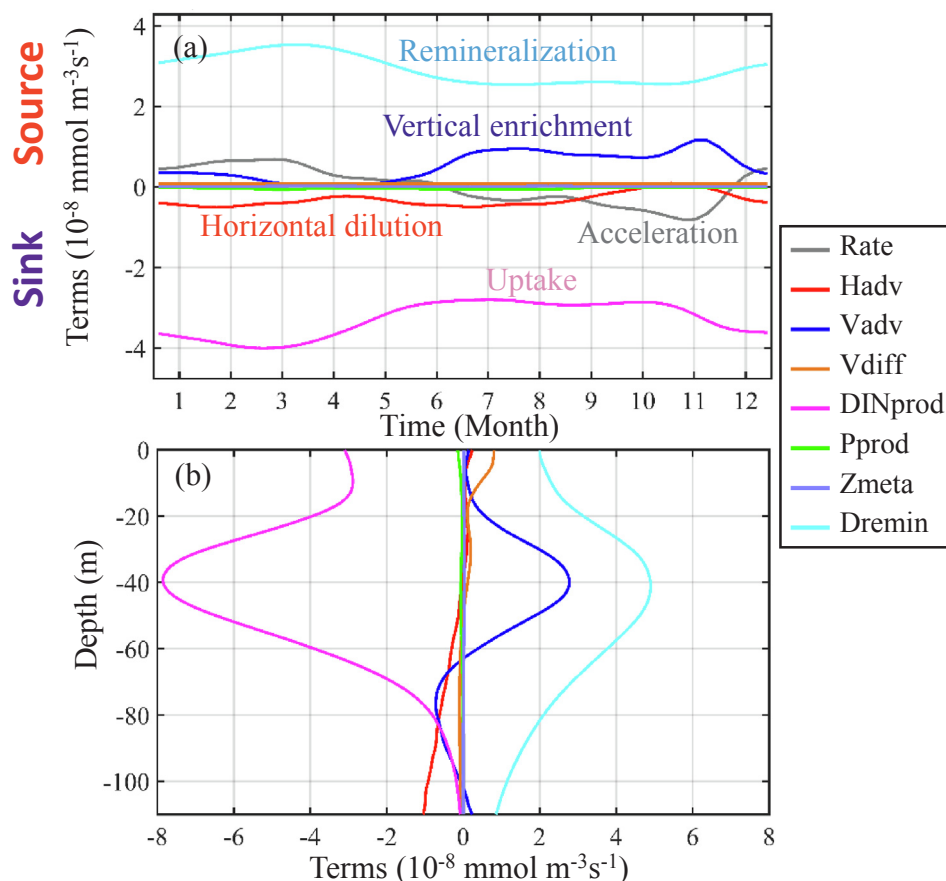


Fig. 16. (a) Time series of volume-averaged terms in the PO₄ equation in the euphotic layer (upper 110 m) of the SCS basin (isobath ≥ 200 m). (b) Vertical profiles of annual mean domain-averaged terms for PO₄ in the basin. The terms are defined in the same way as in Fig. 14.

production, but lagged of ~3 months because detritus takes time to sink from the surface to the deep layer. The main sink of NO₃ was the biological production based on nitrate due to the productive sub-surface chlorophyll maximum layer within the euphotic layer. However, the production was still much lower than the production in the shelf region by totaling production through NO₃ (Nprod) and PO₄ (Pprod). Horizontal advection from adjacent oceans was also an important sink due to dilution by the Kuroshio intrusion as discussed in Section 4.1. The growth of phytoplankton is limited by nitrogen in the open ocean as indicated by Wu et al. (2003). The biological production was higher in winter and early spring, in accordance with the higher nutrient supply during the same period.

Vertical advection was largely balanced by primary production in the upper ~80 m where most of the phytoplankton biomass dwelled (Fig. 15b), which is consistent with the finding of Ning et al. (2004). Nutrients were no longer consumed by primary production at the bottom of the euphotic layer, but nitrification kept replenishing NO₃ down to a greater depth after reaching a maximum at ~80 m. The low remineralization rate, sinking of organic particles (detritus), and light inhibition (as shown by Equation (2)) jointly shaped the vertical distribution of the nitrification term. This also explains why the volume-averaged nitrification peaked in early summer while production reached its maximum in early spring (Fig. 15a); it took time for the detritus to sink to the deep layer where the light condition were more favorable for nitrification. The NO₃ produced during nitrification balanced net advection (horizontal + vertical) below the euphotic layer. The nitrification rate is expressed as

$$n = n_{\max} * \left(1 - \max \left[0, \frac{I - I_0}{k_I + I - I_0} \right] \right) \quad (2)$$

where n_{\max} is the maximum nitrification rate; I_0 is the radiation threshold for nitrification inhibition; and k_I is the half-saturation radiation for nitrification inhibition. The diffusion effect due to mixing was relatively small except near the surface where the wind effect was strong.

The main sink of PO₄ in the euphotic layer was also biological uptake and horizontal advection (Fig. 16). Like in the SCS shelf, remineralization was still the most important source of PO₄ due to its high turnover rate, and, as a result, the advection and diffusion were relatively smaller. The seasonal trend of the volume-averaged remineralization term of PO₄ also followed the seasonal trend of production, but with a slight time lag (Fig. 16a). Remineralization of PO₄ differed from the remineralization of NO₃. The remineralization of PO₄ peaked at nearly the same depth as the production, and it decreased sharply with depth (Fig. 16b).

The nutrient dynamics in terms of biogeochemical processes was weak below upper layer because the biological activities were extremely low. Three-dimensional physical transport regulated the nutrients in the deep layer as reflected in the horizontal and vertical advection. Fig. 17 shows the domain- and depth-integrated terms in the upper, middle, and deep layers. As we discussed previously, physical and biogeochemical processes were equally important as sources and sinks of nutrients in the upper layer, where vertical advection compensated for the strong sink of horizontal advection due to the dilution. However, horizontal advection was the dominant source of nutrients in the deep layer mainly due to the strong intrusion through LS, and horizontal advection was balanced by upward advection into the middle layer. In the middle layer, the outflow through LS exported the SCS waters that had a lower nutrient concentration (Fig. 11), while a downward flux (Liu and Gan, 2017) diluted the nutrient concentration

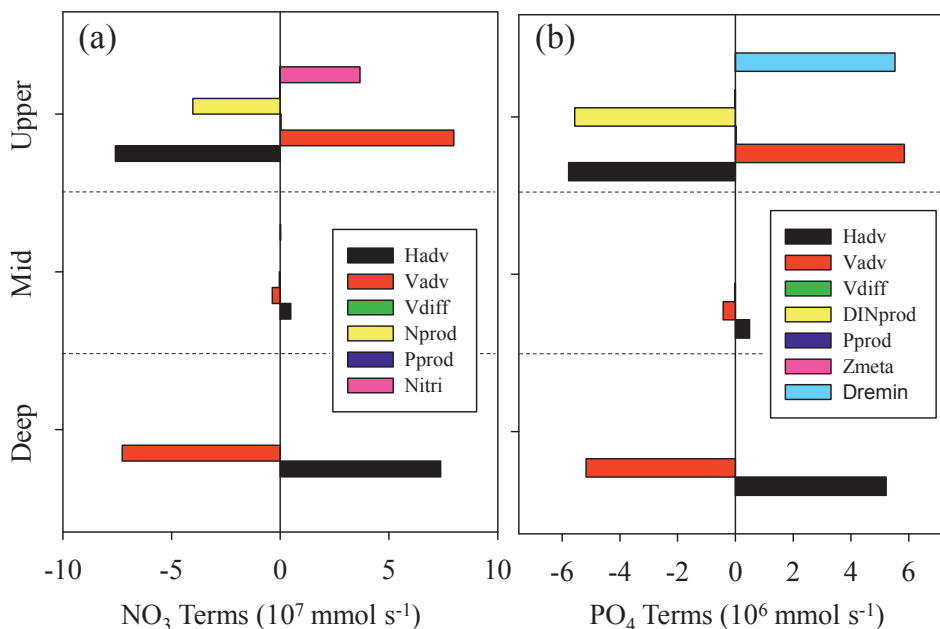


Fig. 17. Domain- and layer-integrated terms in the (a) NO_3 and (b) PO_4 equations in the upper, middle, and deep layers of the SCS basin (isobath ≥ 200 m). The terms are defined in the same way as in Figs. 12 and 13.

in the middle layer, although the magnitudes of both terms were very small.

5. Summary

We developed a coupled physical-biological three-dimensional model that accommodated the biogeochemical characteristics in the deep basin and in shelf waters to investigate the influence of physical and biological processes on nutrient transport and dynamics in the SCS. We based our investigation on field observations and knowledge synthesized from historic studies. Our model satisfactorily captured the observations, and our study provided new insights into the spatio-temporal variation of nutrient distribution, transport, and dynamics in the SCS.

Our analysis demonstrated that organic nutrients must be considered when assessing nutrient transport, especially in shallow and highly productive shelf regions. Considering organic nutrients is essential because the level of labile organic nutrients, comprising marine organisms and their metabolites, can be much higher than the level of dissolved inorganic nutrients.

The vertical structure of nutrients in the SCS was closely related to the inflow-outflow-inflow transport through LS. The upward advection of deep intrusive water that had high nutrient loading compensated for the nutrient deficiency in the upper layer. The Kuroshio intrusion diluted the nutrients in the upper layer so that they decreased from the southwest to the northeast of the basin. Upward advection from deep layer joined the water in the middle layer in the northern basin during the outflow and produced increasing nutrients from the southwest to the northeast. There was subduction over the eastern slope and obduction over the western slope of the southern basin so that the nutrient concentration decreased from the north to the south in the deep layer. The unique three-layered horizontal distribution of nutrients corresponded to the CAC three-layer circulation in the SCS. The three-layer circulation is extrinsically controlled by the sandwich-like transport through LS and exchange through the other straits.

The nutrient transport was jointly regulated by volume transport and gradient of nutrients. The westward upper-layer intrusion through LS was strongest during winter because of a weakened Kuroshio current, but the deep-layer intrusion was stronger in late

summer due to the stronger cyclonic summer circulation in the deep SCS basin. Therefore, the depth-integrated nutrient transport through this strait had a double-peak seasonal pattern.

We analyzed the nutrient dynamics by decomposing the terms in the nutrient balance governing equations. In the shelf waters, vertical advection was the dominant source of NO_3 in the surface-mixed layer because of strong coastal upwelling. Biological production was the main sink where the production through PO_4 was significantly higher than the production through NO_3 during summer. The situation was reversed in winter. This finding demonstrates the alternating influence of the P-limited river plume and the N-limited coastal water. Below the surface mixed layer, the sources of NO_3 from remineralization, upward mixing, and lateral inflow were balanced by biological uptake and upward flux. We attributed the main differences between the balances of PO_4 and NO_3 to the high N:P ratio in the river plume and the high turnover rate of phosphorus.

In the upper layer of the SCS basin, vertical advection and nitrification were the main sources of NO_3 , and the NO_3 is predominantly consumed by production. We identified horizontal advection as another important sink because of the dilution by the intrusion of lower NO_3 waters from the WPO through the LS. Vertically, advection was largely balanced by primary production in the upper ~ 80 m and by nitrification in the deeper layer. The vertical variation in nitrate dynamics was also jointly shaped by the remineralization rate, the sinking of detritus, and light inhibition. The main sinks of PO_4 in the euphotic layer also consisted of biological production and horizontal advection, but the source of PO_4 was detritus remineralization due to the much higher phosphorus turnover rate. For the same reason, there was a much smaller dislocation and time lag between production and remineralization vertically for PO_4 than NO_3 .

Declaration of Competing Interest

None.

Acknowledgements

This research was supported by the National (China) Basic Research Development Program (2015CB954004), Theme-based Research

Scheme (T21-602/16-R), and the General Research Fund (16202514, 16308319) of the Hong Kong Research Grants Council. We are also grateful for the support of The National Supercomputing Center of Tianjin. MODIS (Moderate Resolution Imaging Spectroradiometer) data were obtained from <https://modis.gsfc.nasa.gov> and SeaWiFS (Sea-viewing Wide Field-of-view Sensor) data were obtained from <https://oceancolor.gsfc.nasa.gov/SeaWiFS/>. All numerical results presented in the figures were produced by solving equations in the Regional Ocean Modeling System (ROMS). The source code of ROMS can be downloaded from <https://www.myroms.org/>. Some figures were plotted using Ocean Data View (Schlitzer, R., Ocean Data View, odv.awi.de, 2017).

Appendix A

$$\frac{\partial [N]}{\partial t} = -\mu_{\max} f(I)[Phyto] \left(\sigma_N \frac{[N]}{k_N + [N]} \cdot \frac{1}{1 + [A]/k_A} + \sigma_P \frac{[N]}{[N] + [A]} \cdot \frac{[P]}{k_P + [P]} \right) + n[A] \quad (A1)$$

$$\begin{aligned} \frac{\partial [A]}{\partial t} = & -\mu_{\max} f(I)[Phyto] \left(\sigma_N \frac{[A]}{k_A + [A]} + \sigma_P \frac{[A]}{[N] + [A]} \cdot \frac{[P]}{k_P + [P]} \right) - n[A] \\ & + l_{BM}[Zoo] + l_E \frac{[Phyto]^2}{k_{Phyto} + [Phyto]^2} \beta [Zoo] + r_{SDN}[SDN] + r_{LDN}[LDN] \end{aligned} \quad (A2)$$

$$\begin{aligned} \frac{\partial [P]}{\partial t} = & -\mu_{\max} f(I)[Phyto] \left(\sigma_N \left(\frac{[N]}{k_N + [N]} \cdot \frac{1}{1 + [A]/k_A} + \frac{[A]}{k_A + [A]} \right) r_{PN} + \sigma_P \frac{[P]}{k_P + [P]} r_{PN} \right) \\ & + l_{BM} r_{PN}[Zoo] + l_E r_{PN} \frac{[Phyto]^2}{k_{Phyto} + [Phyto]^2} \beta [Zoo] + r_{SDP}[SDP] + r_{LDP}[LDP] \end{aligned} \quad (A3)$$

where N , A , P , $Phyto$, Zoo , SDN , LDN , SDP , and LDP represent NO_3 , NH_4 , PO_4 , phytoplankton, zooplankton, N-fraction of small detritus, N-fraction of large detritus, P-fraction of small detritus, and P-fraction of large detritus, respectively. μ_{\max} is the maximum growth rate of phytoplankton under a given temperature T (Eppley, 1972). $f(I)$ represents the photosynthesis-light (P-I) relationship. σ_N and σ_P are nutrient limitation coefficients. k_N , k_A and k_P are half-saturation constants for phytoplankton uptake of NO_3 , NH_4 , and PO_4 , respectively. n is the nitrification rate that is regulated by light (Olson, 1981). K_{Phyto} is the zooplankton half-saturation constant for ingestion. l_{BM} is the zooplankton basal metabolism. l_E is the zooplankton-specific excretion rate. β is the zooplankton assimilation efficiency for nitrogen. r_{PN} is the cellular P:N ratio, and r_{SDN} , r_{LDN} , r_{SDP} , and r_{LDP} are the small/large detritus remineralization rates for nitrogen/phosphorus. Detailed biochemical processes and dynamics are found in Gan et al. (2014).

References

- Cai, W.J., Dai, M.H., Wang, Y.C., Zhai, W.D., Huang, T., Chen, S.T., Zhang, F., Chen, Z.Z., Wang, Z.H., 2004. The biogeochemistry of inorganic carbon and nutrients in the Pearl River estuary and the adjacent Northern South China Sea. *Cont. Shelf Res.* 24 (12), 1301–1319.
- Chai, F., Liu, G.M., Xue, H.J., Shi, L., Chao, Y., Tseng, C.M., Chou, W.C., Liu, K.K., 2009. Seasonal and Interannual Variability of Carbon Cycle in South China Sea: A Three-Dimensional Physical-Biogeochemical Modeling Study. *J. Oceanogr.* 65 (5), 703–720.
- Chen, C.T.A., 2008. Distributions of nutrients in the East China Sea and the South China Sea connection. *J. Oceanogr.* 64 (5), 737–751.
- Chen, C.T.A., Wang, S.L., Wang, B.J., Pai, S.C., 2001. Nutrient budgets for the South China Sea basin. *Mar. Chem.* 75 (4), 281–300.
- Chen, Y.F.L., 2005. Spatial and seasonal variations of nitrate-based new production and primary production in the South China Sea. *Deep-Sea Research I* 52 (2), 319–340. <https://doi.org/10.1016/j.dsr.2004.11.001>.
- Chiang, T.L., Hsin, Y.C., Wu, C.R., 2018. Multidecadal Changes of Upper-Ocean Thermal Conditions in the Tropical Northwest Pacific Ocean versus South China Sea during 1960–2015. *J. Clim.* 31 (10), 3999–4016.
- Chou, Wen-Chen, Sheu, David D., Chen, C. T. Arthur, Wen, Liang-Saw, Yang, Yih, Wei, Ching-Ling, 2007. Transport of the South China Sea subsurface water outflow and its influence on carbon chemistry of Kuroshio waters off southeastern Taiwan. *J. Geophys. Res.* 112 (C12). <https://doi.org/10.1029/2007JC004087>.
- Dai, A., Trenberth, K.E., 2002. Estimates of freshwater discharge from continents: latitudinal and seasonal variations. *J. of Hydrometeorology* 3 (6), 660–687.
- Dai, M.H., Zhai, W.D., Cai, W.J., Callahan, J., Huang, B.Q., Shang, S.L., Huang, T., Li, X.L., Lu, Z.M., Chen, W.F., Chen, Z.Z., 2008. Effects of an estuarine plume-associated bloom on the carbonate system in the lower reaches of the Pearl River estuary and the coastal zone of the northern South China Sea. *Cont. Shelf Res.* 28 (12), 1416–1423. <https://doi.org/10.1016/j.csr.2007.04.018>.
- Du, C., Liu, Z., Dai, M., Kao, S.J., Cao, Z., Zhang, Y., Huang, T., Wang, L., Li, Y., 2013. Impact of the Kuroshio intrusion on the nutrient inventory in the upper northern South China Sea: insights from an isopycnal mixing model. *Biogeosciences* 10 (10), 6419–6432.
- Duan, S.W., Liang, T., Zhang, S., Wang, L.J., Zhang, X.M., Chen, X.B., 2008. Seasonal changes in nitrogen and phosphorus transport in the lower Changjiang River before the construction of the Three Gorges Dam. *Estuar. Coast. Shelf Sci.* 79 (2), 239–250.
- Dyhrman, S.T., Ammerman, J.W., Van Mooy, B.A.S., 2007. Microbes and the marine phosphorus cycle. *Oceanography* 20 (2), 110–116.
- Eppley, R.W., 1972. Temperature and phytoplankton growth in sea. *Fishery Bulletin.* 70 (4), 1063–1085.
- Fasham, M.J.R., Ducklow, H.W., McKelvie, S.M., 1990. A nitrogen-based model of plankton dynamics in the oceanic mixed layer. *J. Mar. Res.* 48, 591–639.
- Fennel, K., Wilkin, J., Levin, J., Moisan, J., O'Reilly, J., Haidvogel, D., 2006. Nitrogen cycling in the Middle Atlantic Bight: results from a three-dimensional model and implications for the North Atlantic nitrogen budget. *Global Biogeochem. Cy.* 20 (3) GB3007, [10.1029/2005gb002456](https://doi.org/10.1029/2005gb002456).
- Gan, J., Qu, T., 2008. Coastal jet separation and associated flow variability in the southwest South China Sea. *Deep-Sea Res Pt I* 55 (1), 1–19.
- Gan, J., Li, H., Curchitser, E.N., Haidvogel, D.B., 2006. Modeling South China sea circulation: response to seasonal forcing regimes. *J. Geophys. Res.-Oceans* 111 (C6), C06034 [10.1029/2005JC003298](https://doi.org/10.1029/2005JC003298).
- Gan, J., Cheung, A., Guo, X.G., Li, L., 2009a. Intensified upwelling over a widened shelf in the northeastern South China Sea. *J. Geophys. Res. -Oceans* 114. <https://doi.org/10.1029/2007jc004660>.
- Gan, J., Li, L., Wang, D.X., Guo, X.G., 2009b. Interaction of a river plume with coastal upwelling in the northeastern South China Sea. *Cont. Shelf Res.* 29 (4), 728–740. <https://doi.org/10.1016/j.csr.2008.12.002>.
- Gan, J., Lu, Z.M., Dai, M.H., Cheung, A., Harrison, P., Liu, H.B., 2010. Biological response to intensified upwelling and to a river plume in the northeastern South China Sea: A modeling study. *J. Geophys. Res. -Oceans* 115, C09001. <https://doi.org/10.1029/2009JC005569>.
- Gan, J., Liu, Z.Q., Liang, L.L., 2016a. Numerical modeling of intrinsically and extrinsically forced seasonal circulation in the China Seas: a kinematics study. *J. Geophys. Res. -Oceans.* <https://doi.org/10.1002/2016JC011800>.
- Gan, J., Liu, Z.Q., Hui, C.R., 2016b. A three-layer alternating spinning circulation in the South China Sea. *J. Phys. Oceanogr.* 46 (8), 2309–2315. <https://doi.org/10.1175/JPO-D-16-0044.1>.
- Gan, J., Lu, Z.M., Cheung, A., Dai, M., Liang, L.L., Harrison, P.J., Zhao, X.Z., 2014. Assessing ecosystem response to phosphorus and nitrogen limitation in the Pearl River plume using the Regional Ocean Modeling System (ROMS). *J. Geophys. Res. -Oceans* 119. <https://doi.org/10.1002/2014JC009951>.
- Gong, G.C., Liu, K.K., Liu, C.T., Pai, S.C., 1992. The chemical hydrography of the South China Sea west of Luzon and a comparison with the West Philippine Sea. *Terr Atmos Ocean Sci* 3, 587–602.
- Gordon, H.R., McCluney, W.R., 1975. Estimation of Depth of Sunlight Penetration in Sea for Remote-Sensing. *Appl. Optics* 14 (2), 413–416.
- Han, A.Q., Dai, M.H., Gan, J., Kao, S.J., Zhao, X.Z., Jan, S., Li, Q., Lin, H., Chen, C.T.A., Wang, L., Hu, J.Y., Wang, L.F., Gong, F., 2013. Inter-shelf nutrient transport from the East China Sea as a major nutrient source supporting winter primary production on the northeast South China Sea shelf. *Biogeosciences* 10 (12), 8159–8170. <https://doi.org/10.5194/bg-10-8159-2013>.
- Hopkinson, C.S., Vallino, J.J., Nolin, A., 2002. Decomposition of dissolved organic matter from the continental margin. *Deep-Sea Res Pt II* 49 (20), 4461–4478.
- Lee, Z.P., Hu, C.M., Shang, S.L., Du, K.P., Lewis, M., Arnone, R., Brewin, R., 2013. Penetration of UV-visible solar radiation in the global oceans: Insights from ocean color remote sensing: PENETRATION OF UV-VISIBLE SOLAR LIGHT. *J. Geophys. Res. -Oceans* 118 (9), 4241–4255. <https://doi.org/10.1002/jgrc.20308>.
- Liu, K.K., Tseng, C.M., Wu, C.R., Lin, I.I., 2010a. Carbon and Nutrient Fluxes in Continental Margins: A Global Synthesis. Springer, Berlin.
- Liu, S.M., Guo, X.Y., Chen, Q., Zhang, J., Bi, Y.F., Luo, X., Li, J.B., 2010b. Nutrient dynamics in the winter thermohaline frontal zone of the northern shelf region of the South China Sea. *J. Geophys. Res.-Oceans*, pp. 115.

- Liu, Z.Q., Gan, J., 2016. Open boundary conditions for tidally and subtidally forced circulation in a limited-area coastal model using the Regional Ocean Modeling System (ROMS). *J. Geophys. Res.-Oceans* 121 (8), 6184–6203.
- Liu, Z.Q., Gan, J., 2017. Three-dimensional pathways of water masses in the South China Sea: A modeling study. *J. Geophys. Res.-Oceans*. <https://doi.org/10.1002/2016JC012511>.
- Meybeck, M., 1982. Carbon, nitrogen, and phosphorus transport by world rivers. *Am. J. Sci.* 282 (4), 401–450.
- Morel, A., Berthon, J.F., 1989. Surface pigments, algal biomass profiles, and potential production of the euphotic layer - relationships reinvestigated in view of remote-sensing applications. *Limnol. Oceanogr.* 34 (8), 1545–1562.
- Ning, X., Chai, F., Xue, H., Cai, Y., Liu, C., Shi, J., 2004. Physical-biological oceanographic coupling influencing phytoplankton and primary production in the South China Sea. *J. Geophys. Res.-Oceans* 109 (C10). <https://doi.org/10.1029/2004JC002365>.
- Ogawa, H., Tanoue, E., 2003. Dissolved organic matter in oceanic waters. *J. Oceanogr.* 59 (2), 129–147.
- Olson, R.J., 1981. Differential Photoinhibition of Marine Nitrifying Bacteria - a Possible Mechanism for the Formation of the Primary Nitrite Maximum. *J. Mar. Res.* 39 (2), 227–238.
- Qu, T.D., 2000. Upper-layer circulation in the South China Sea. *J. Phys. Oceanogr.* 30 (6), 1450–1460.
- Qu, T.D., 2001. Role of ocean dynamics in determining the mean seasonal cycle of the South China Sea surface temperature. *J. Geophys. Res.-Oceans* 106 (C4), 6943–6955.
- Ruddick, K.G., Gons, H.J., Rijkeboer, M., Tilstone, G., 2001. Optical remote sensing of chlorophyll a in case 2 waters by use of an adaptive two-band algorithm with optimal error properties. *Appl. Optics* 40 (21), 3575–3585.
- Santos, M.L.S., Muniz, K., Barros-Neto, B., Araujo, M., 2008. Nutrient and phytoplankton biomass in the Amazon River shelf waters. *An Acad. Bras. Cienc.* 80 (4), 703–717.
- Shang, S.L., Lee, Z.P., Wei, G.M., 2011. Characterization of MODIS-derived euphotic zone depth: Results for the China Sea. *Remote Sens. Environ.* 115 (1), 180–186.
- Shaw, P.T., Chao, S.Y., 1994. Surface Circulation in the South China Sea. *Deep-Sea Res Pt I* 41 (11–12), 1663–1683.
- Shaw, P.T., Chao, S.Y., Liu, K.K., Pai, S.C., Liu, C.T., 1996. Winter upwelling off Luzon in the northeastern South China Sea. *J. Geophys. Res.-Oceans* 101 (C7), 16435–16448.
- Shchepetkin, A.F., McWilliams, J.C., 2005. The regional oceanic modeling system (ROMS): a split-explicit, free-surface, topography-following-coordinate oceanic model. *Ocean Model.* 9 (4), 347–404. <https://doi.org/10.1016/j.ocemod.2004.08.002>.
- Smith, R.C., 1981. Remote-Sensing and Depth Distribution of Ocean Chlorophyll. *Mar. Ecol. Prog. Ser.* 5 (3), 359–361.
- Spitz, Y.H., Allen, J.S., Gan, J., 2005. Modeling of ecosystem processes on the Oregon shelf during the 2001 summer upwelling. *J. Geophys. Res.-Oceans* 110 (C10), C10S17. <https://doi.org/10.1029/2005JC002870>.
- Wong, G.T.F., Tseng, C.M., Wen, L.S., Chung, S.W., 2007a. Nutrient dynamics and N-anomaly at the SEATS station. *Deep-Sea Res Pt II* 54 (14–15), 1528–1545.
- Wong, G.T.F., Ku, T.L., Mulholland, M., Tseng, C.M., Wang, D.P., 2007b. The SouthEast Asian time-series study (SEATS) and the biogeochemistry of the South China Sea - An overview. *Deep-Sea Res. II* 54 (14–15), 1434–1447. <https://doi.org/10.1016/j.dsr2.2007.05.012>.
- Wong, G.T.F., Pan, X.J., Li, K.Y., Shiah, F.K., Ho, T.Y., Guo, X.H., 2015. Hydrography and nutrient dynamics in the Northern South China Sea Shelf-sea (NoSoCS). *Deep-Sea Res. Pt. II* 117, 23–40.
- Wu, J.F., Chung, S.W., Wen, L.S., Liu, K.K., Chen, Y.L.L., Chen, H.Y., Karl, D.M., 2003. Dissolved inorganic phosphorus, dissolved iron, and Trichodesmium in the oligotrophic South China Sea. *Global Biogeochem. Cy.* 17 (1), 1008 1010.1029/2002GB001924.
- Wyrtki, K., 1961. Physical oceanography of the southeast Asian waters. Scientific results of marine investigations of the South China and the Gulf of Thailand, NAGA Rep., 195 pp, Scripps Institution of Oceanography, La Jolla, Calif.
- Xu, M.N.N., Wu, Y.H., Zheng, L.W., Zheng, Z.Z., Zhao, H.D., Laws, E.A., Kao, S.J., 2017. Quantification of multiple simultaneously occurring nitrogen flows in the euphotic ocean. *Biogeosciences* 14 (4), 1021–1038.
- Yool, A., Martin, A.P., Fernandez, C., Clark, D.R., 2007. The significance of nitrification for oceanic new production. *Nature* 447 (7147), 999–1002.
- Zhai, W., Dai, M., Cai, W.-J., Wang, Y., Wang, Z., 2005. High partial pressure of CO₂ and its maintaining mechanism in a subtropical estuary: the Pearl River estuary, China. *Mar. Chem.* 93, 21–32.
- Zhang, J., Liu, S.M., Ren, J.L., Wu, Y., Zhang, G.L., 2007. Nutrient gradients from the eutrophic Changjiang (Yangtze River) Estuary to the oligotrophic Kuroshio waters and re-evaluation of budgets for the East China Sea Shelf. *Prog. Oceanogr.* 74 (4), 449–478. <https://doi.org/10.1016/j.pocean.2007.04.019>.
- Zhou, K.B., Dai, M.H., Kao, S.J., Wang, L., Xiu, P., Chai, F., Tian, J.W., Liu, Y., 2013. Apparent enhancement of Th-234-based particle export associated with anticyclonic eddies. *Earth Planet Sc Lett* 381, 198–209.
- Zuo, J.L., Song, J.M., Yuan, H.M., Li, X.G., Li, N., Duan, L.Q., 2016. Particulate nitrogen and phosphorus in the East China Sea and its adjacent Kuroshio waters and evaluation of budgets for the East China Sea Shelf. *Cont. Shelf Res.* 131, 1–11.